5-5-2012

High Speed Atomic Force Microscopy Techniques for the Efficient Study of Nanotribology

James L. Bosse
University of Connecticut - Storrs, jlb05013@gmail.com

High Speed Atomic Force Microscopy Techniques for the Efficient Study of Nanotribology

James Louis Bosse

B.S. University of Connecticut, 2009

A Thesis

Submitted in Partial Fulfillment of the

Requirements for the Degree of

Master of Science

at the

University of Connecticut

2012

APPROVAL PAGE

Master of Science Thesis

High Speed Atomic Force Microscopy Techniques for the

Efficient Study of Nanotribology

Presented by

James Louis Bosse, B.S.

Major Advisor _____

Bryan D. Huey

Associate Advisor _____

S. Pamir Alpay

Associate Advisor _____

Harris Marcus

University of Connecticut

2012

Acknowledgements

First, I would like to thank my advisor Dr. Bryan D. Huey for teaching all aspects of the AFM, as well as the continued guidance and mentoring that it takes to become a leader. He always brings out the best of my abilities, and if it wasn't for him, I would not have returned to graduate school from industry.

I would like to thank Dr. Sungjun Lee for programming the AFM to collect the high speed data that I acquired in these experiments. I would like to thank our sample providers, Andreas Andersen and Duncan Sunderland. I would like to thank Jeff Honeyman, Anil Gannepalli, and Jason Bemis at Asylum Research for their help with programming within the AFM software, and Qingzong Tseng for programming the drift correction.

I would like to thank my mentor, friend, and former group member, Dr. Nicholas Polomoff. He has helped me with many aspects of research and life lessons.

Lastly, I would like to thank the current Huey group members for their support: Dr. Varun Vyas, Linghan Ye, Joshua Leveillee, Alejandro Lluberes, Atif Rakin, Vincent Palumbo, Gregory Santone, and Yasemin Kutes.

Funding from NSF:DMR:IMR award 0817263 is recognized for the acquisition and development of the high speed AFM system employed in this research. Ongoing student support is recognized from NSF-DMR-MWN award 0909091.

List of Figures

Table of Contents

Abstract

As mechanical devices scale down to micro/nano length scales, it is crucial to understand friction and wear at the nanoscale (nanotribology) especially at technically relevant sliding velocities. Accordingly, three novel techniques have been developed to study nanotribology, leveraging recent advances in high speed AFM. The first method utilizes high line-scanning rates coupled with sinusoidal scanning along the AFM fast scan axis, enabling rapid friction measurements as a function of velocity up to 20 mm/sec. The second method rapidly acquires friction versus force curves through disabling the feedback loop during scanning and relating the resulting lateral data with the correspondingly varying normal loads. The third and most widely applicable technique rapidly creates a map of friction-force curves based on a sequence of high speed images each with incrementally lower loads. As a result, 'images' of the coefficient of friction, friction at zero load, and/or load for zero friction (typically adhesive) can be uniquely determined for heterogeneous surfaces. This work includes measurements on mica, nanocrystalline diamond, and Au/SiO_2 micro-fabricated structures, and is applicable for wear of sliding or rolling components in MEMS, biological implants, contact lenses, data storage devices, etc.

The sinusoidal scanning technique allows friction force measurements in two dimensions to be acquired faster than any system currently on the market. The high scan velocity friction properties of mica have been characterized, and viscous damping forces between the cantilever and substrate dominate in agreement with the thermally-activated Eyring and Tomlinson models. Friction force curves are also extracted at any scan velocity along the line scan, allowing less experimental time to acquire such a broad range of

equivalent friction data. Friction force curves collected with a disabled vertical feedback loop allow for the rapid characterization of substrates with either low or high varying topographies. The theory has been demonstrated on a silica characterization grating, allowing the coefficient of friction, friction at zero applied force, and pull-off force to be extracted. Finally, an array of friction force curves was acquired on a SiO_2/thiol substrate at a scanning velocity approaching 3 mm/s. The coefficient of friction and friction at zero applied force were determined for the SiO_2 phase and the thiol phases, and were equivalent to the coefficients acquired at normal scan rates, approximately 300 times slower. Not limited to high scan velocities, the importance of this approach is that friction can be mapped for specimens with defects, topographic features, and/or phase differences at the micro- and nano- scale.

Chapter 1: Introduction

1.1 Overview: The Study of Tribology

The study of friction and the related phenomena of wear, adhesion, and lubrication are known as tribology. Design processes for materials and sliding interfaces have been studied for centuries to decrease or increase friction, depending on the application. One such example is our daily commute; the coefficient of friction of rubber on a dry road is approximately 0.8, 0.25 when wet, and .15 on ice[1]. Without this difference in the coefficient of friction, the necessary research and development for tire safety would be much smaller than it is today. Friction not only plays a large role in the design process of engineered materials, but in our daily lives as well. The joints in our body are in use for decades, yet maintain a friction coefficient of only .02[2]. Another example of tribology in our daily lives is shaving. Technology has developed from the copper, bronze, and iron of olden times, to the steel and Teflon coated blades of the present. Our dry skin, with a coefficient of friction of approximately .49, has been the target for reduction of many lubricants and creams used for shaving[2].

The study of tribology is also valid for the design of micro- and nanoelectromechanical systems (MEMS/NEMS). Currently, there are no sliding components in these devices due to the high adhesion forces at small length scales[3-5]. The study of nanotribology aims to understand and control these forces, and is principally conducted with atomic force microscope (AFM) systems. However, most MEMS/NEMS operate at velocities of meters per second or faster, higher than the reproducible characterization velocity of

AFM systems[6]. Accordingly, tremendous effort is being spent to improve atomic force scanning systems for the study of nanotribology at technically relevant velocities.

1.2 Atomic Force Microscopy

The atomic force microscope (AFM) has been a crucial instrument for the study of nanotribology because the system resolution is capable of measuring forces down to the atomic scale. The first AFM was invented in 1986 by Binnig, Quate, and Gerber[7]. The system combines the principles of the scanning tunneling microscope and the stylus profilometer to measure sample topography with a vertical resolution of 1 Å and a lateral resolution of 10 Å. A probe tip with a small radius of curvature, between 10 nm and 1 μm is attached to a cantilever beam and interacted with the surface.

One of two primary modes is typically implemented in AFM. Contact mode applies a constant repulsive force between the tip and the sample, detected by simple deflection of the integrated cantilever beam. AC or 'tapping mode'™ imaging oscillates the AFM probe at the cantilever beam's resonant frequency to apply a constant force gradient (repulsive, or attractive). The resonant frequency of the beam is given by the function $f_0 = (1/2\pi)(k_c / m_0)^{1/2}$ where k_c is the spring constant and m_o is the effective mass. This resonant frequency will shift as the force increases between the probe and sample surface. Such a force will cause the cantilever to deflect, but force gradients can be detected much more sensitively by monitoring the lever resonance frequency, amplitude, or phase with respect to the oscillatory driving signal.

To control the probe and/or sample position, a piezoelectric drive capable of controlling motion in the x, y, and z directions is attached to the sample or tip stage. Upon engaging a feedback loop, a constant deflection, or resonance, is then maintained by continuously

updating the tip-sample indentation/separation with sub-nanometer scale precision. One of the weakest inter-atomic forces is considered the van der Waals bond, which is on the order of 10^{-11} to 10^{-12} N. The AFM is capable of measuring forces as low as 10^{-18} N, far less than that necessary to capture such inter-atomic forces.

To achieve such high resolution, and expand the general applicability of this initially vacuum-based technique, further improvements were made in 1988 by Meyer and Amer in which the cantilever deflection was detected optically[8]. This simple technique replaced the complicated tunneling junction from the STM probe while retaining the spatial resolution of the original AFM. With the optical method, a laser beam or LED is reflected off the back of the cantilever into a split position sensitive detector (PSD). As the normal force between the probe and sample changes due to inter-atomic forces, the cantilever deflects. A sketch of the optical beam method is presented in Figure 1.

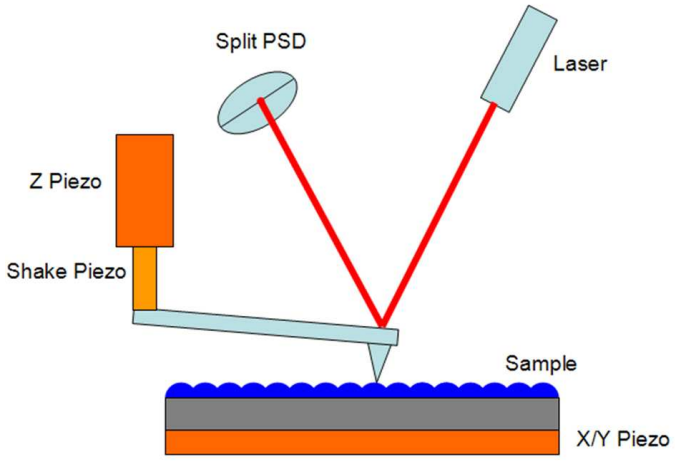

Figure 1: Schematic of the optical beam method for the AFM. Laser light is reflected off of the cantilever to the split position sensitive detector. The shake piezo oscillates the cantilever at its resonant frequency when operating in AC-mode. The z-piezo functions to maintain a constant interaction between the probe and surface.

The optical beam method is sensitive enough to be operated in the repulsive regime or the attractive regime of the inter-atomic potential. When the AFM is being operated in the

repulsive regime, the force between the AFM probe and the sample is given by the equation $F = k_c \Delta z$, where Δz is the vertical deflection of the cantilever and *k* is the spring constant. As the vertical deflection of the cantilever changes with inter-atomic force, the position of the laser spot on the PSD moves up or down. As before, a piezoelectric feedback loop which controls x, y, and z motion is then used to keep the force constant between the tip and sample.

1.3 Lateral Force Microscopy

One additional early scanning technique discovered for the AFM was by Mate et al. in 1987, known as lateral force microscopy (LFM). Using the atomic force microscope, they slid a tungsten wire across the basal plane of a graphite surface at low loads, less than 10^{-4} N, and the friction force observed displayed the periodicity of the atomic surface[9]. The tungsten wire was slid across the surface at three different forces, and over a range of velocities. The frictional forces show a negligible correlation to velocity over the range of 40 Å/s to 4000 Å/s. At the lowest load between the graphite sample and the tungsten wire, a small friction force can be seen. As the force is increased to 2.4×10^{-5} N the friction force shows a corrugation with periodicity of 2.5 Å, which is the same distance between each hexagon-shaped atomic structure. Figure 2 presents the friction as a function of applied load.

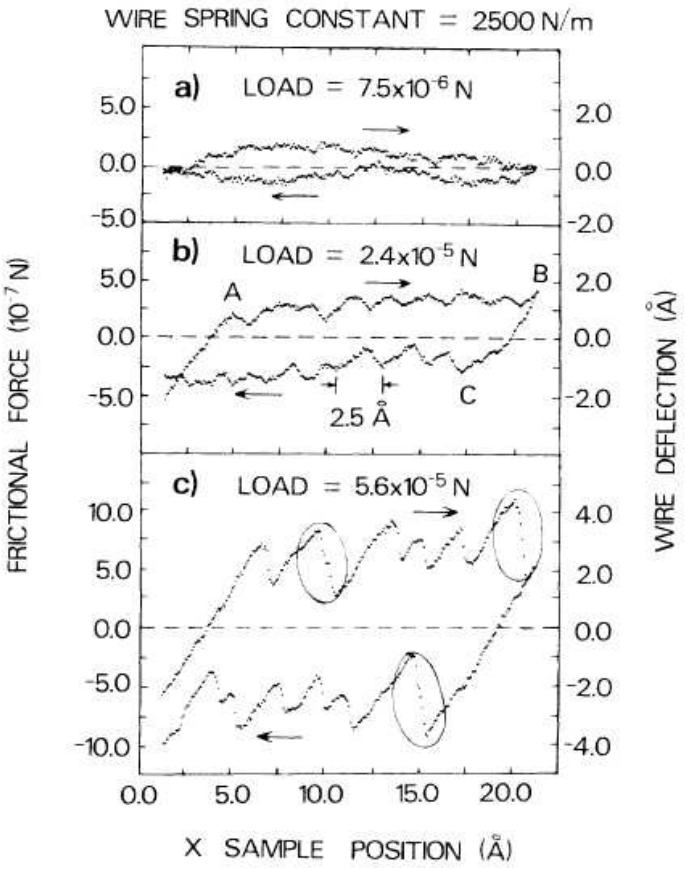

Figure 2: Friction as a function of applied load for a tungsten wire with spring constant 2500 N/m sliding across a graphite substrate. a) The load applied produces minimal friction forces. b) the appearance of a periodic friction force is apparent c) there is a clear periodic transition between static friction and kinetic friction, known as stick-slip, highlighted by the circles[9].

Each corrugation in the graph correlates to a transition known as the stick-slip phenomenon, which is the transition between static friction and kinetic friction at the atomic scale. In a standard model of friction, the friction is assumed to be proportional to the area of contact by the equation $F = sA$, where F is the friction force, s is the shear strength of the interface between two surfaces, and A is the actual area of contact[10]. For materials where the interface of contact is only the apexes of asperities, the area of contact is proportional to load. This was observed experimentally by Mate et al. and is presented in Figure 3.

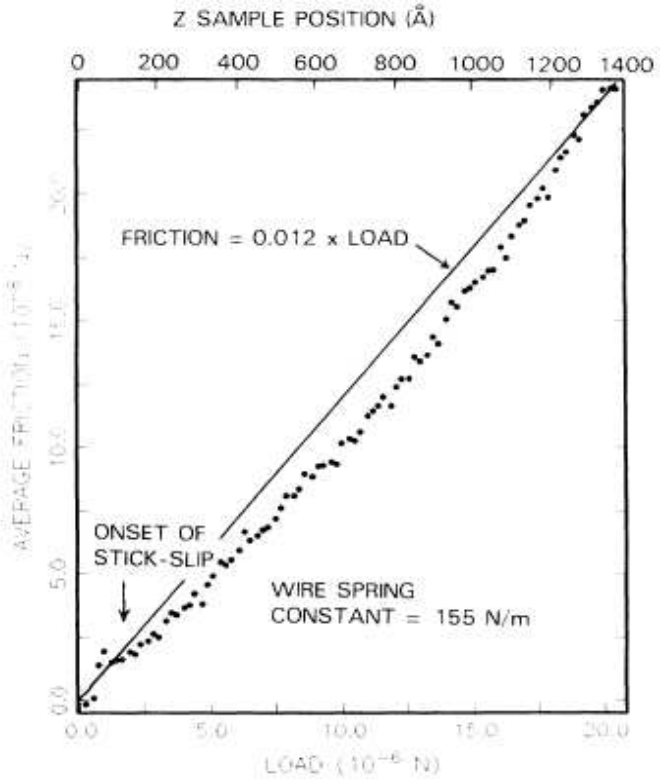

Figure 3: Friction force as a function of load for a tungsten wire on graphite[9]. The plot has a line fit with slope representing the coefficient of friction of .012

The development of lateral force microscopy was improved further in 1990 by Marti et al. by simultaneously measuring the force normal to the sample surface and the friction force[11]. Previous optical methods utilized a split photodiode which measures the optical reflection along one axis, either vertically for topography, or laterally for friction. By replacing the split photodiode with a quadrant photodiode, the deflection due to normal force and the twisting due to friction force can be measured at the same time.

Since the traditional optical beam method was implemented in AFM, micro-machined cantilevers have been primarily fabricated out of Silicon or Si_3N_4. These cantilevers allow the loading of the tip, or the normal force, to be at least 50 times lower that investigated by Mate et al. Lateral forces with a resolution below 1 nN were also achievable.

1.4 Lateral Calibration

The AFM can provide characterization of friction properties on the nanoscale for a variety of surfaces. However, in order to accurately reproduce the data in a quantitative manner, the cantilevers used must be calibrated to determine the ratio of lateral twisting to normal deflection. The "Wedge method" was developed in 1996 by Ogletree, Carpick, and Salmeron to calibrate the cantilever by scanning the tip across a surface of two different known slopes, and analyzing both the topography and friction forces that were collected[12]. The sample used by Ogletree et al. was a faceted $SrTiO_3$ (305) surface, which was annealed in oxygen to reveal two distinct planes with angles of 14 degrees for the (101) plane, and 12.5 degrees for the (103) plane[13]. This is presented in Figure 4.

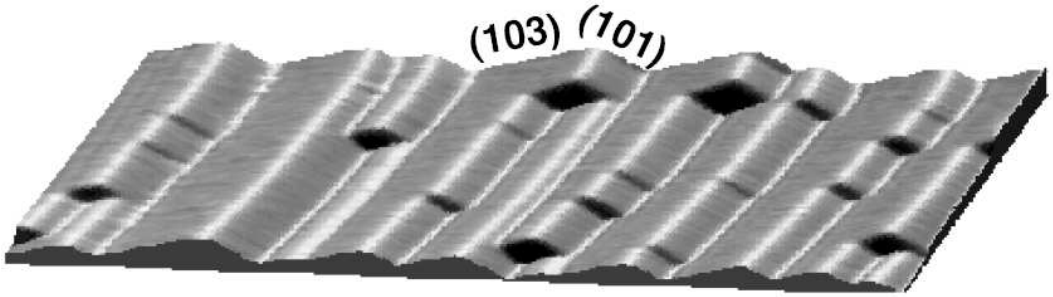

Figure 4: AFM topography image showing the (103) plane and the (101) plane of $SrTiO_3$ used for lateral calibration of an AFM cantilever[13].

Experimentally, the lateral output is measured as a voltage, which is related to the lateral force by the equation $T = \alpha T_0$, where T is the output in Newtons, α is the lateral calibration factor in Newtons per volt, and T_0 is the experimentally acquired lateral output in volts. The lateral calibration factor depends on all of the factors in the experiment, including the lateral spring constant, normal spring constant, the sensitivity of the quadrant photodiode, and the ratio of normal to lateral forces on the sloped surfaces.

Figure 5 presents three distinct lateral force signals acquired on a surface with no slope, a surface with positive slope, and a surface with negative slope.

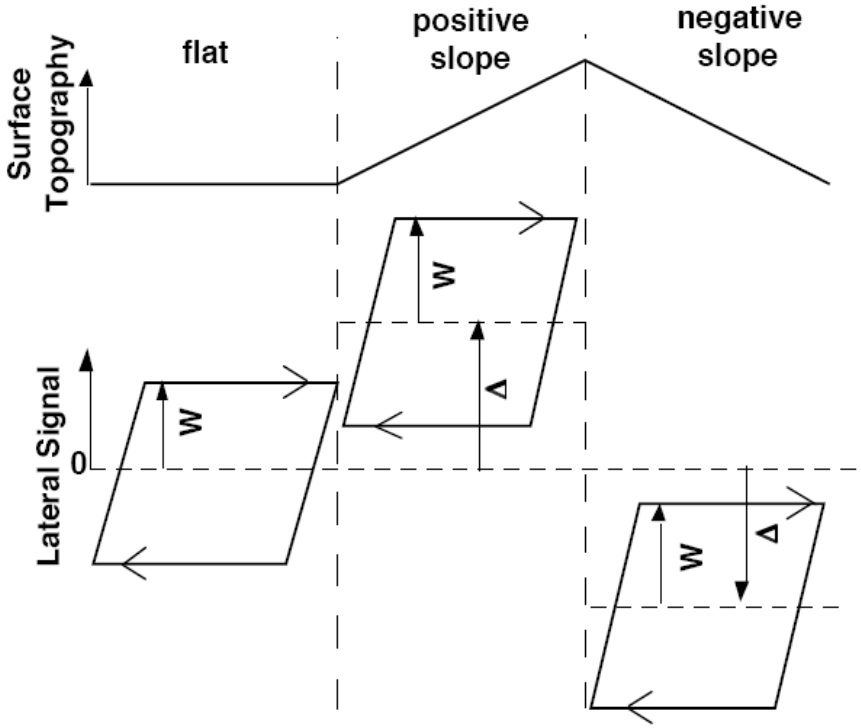

Figure 5: The lateral signal acquired for surfaces with three different slopes (flat, positive slope, and negative slope). W is the friction loop half-width, which varies slightly for all three surfaces. The delta is the offset of the lateral signal which is based on the tilt of each surface[12].

In each of the three cases, the arrow in the right direction represents the "trace" of each image, or the tip scanning across the surface from left to right. The arrow in the left direction represents the "retrace" of each image, or the tip scanning across the surface from right to left. Assuming the sample is homogeneous in terms of its friction coefficient, the half-width of this "friction loop" is dependent on the topography and on the normal load applied, W(L). The offset of the friction loop on a sloped surface from the friction loop on a flat surface is known as the friction loop offset, Δ(L), which depends on normal load as well. The experimentally acquired quantities are in volts, and are designated as W_0 and Δ_0. To acquire the lateral force calibration constant, α, the

friction loop half-width and the friction loop offset is acquired for many different loads, ranging from negligible normal force to very high normal force. These friction loop widths and offsets are plotted on a graph versus normal load, as shown in Figure 6.

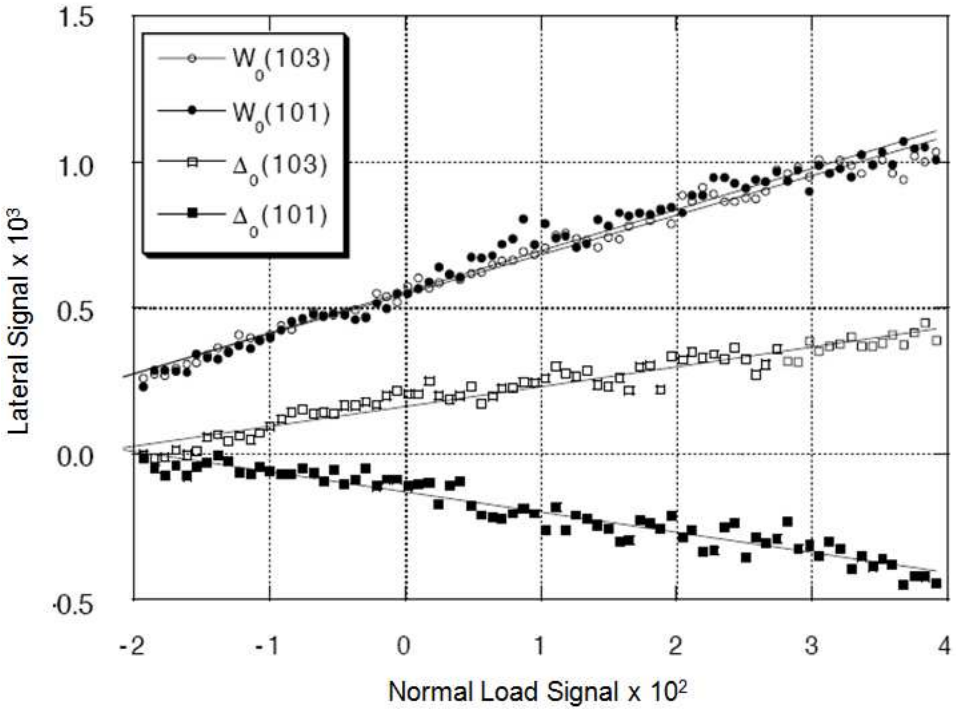

Figure 6: Friction loop half-width and offset plotted as a function of normal load for a faceted $SrTiO_3$ (305) surface with (101) and (103) planes[12].

Once these plots are acquired, they can be fit with lines as shown above. The slopes of these lines represent the change in friction loop half-width and friction loop offset with applied load. The relations for friction loop half-width and friction loop offset are $W_0' = \partial W_0 / \partial L_0$ and $\Delta_0' = \partial \Delta_0 / \partial L_0$, respectively. Ogletree et al. derived an expression to relate these experimentally acquired values to the tip-surface friction coefficient, μ, by the equation:

$$\mu + \frac{1}{\mu} = \frac{2\Delta_0'}{W_0' \sin 2\theta} \tag{1.3.1}$$

where θ is the angle of the tilted surface. Once the coefficient of friction is known, the lateral calibration constant can be found by solving either of the following equations:

$$\alpha/\beta \cdot \Delta_0' = \Delta' = \frac{(1+\mu^2)\sin\theta\cos\theta}{\cos^2\theta - \mu^2\sin^2\theta} \tag{1.3.2}$$

$$\alpha/\beta \cdot W_0' = W' = \frac{\mu}{\cos^2\theta - \mu^2\sin^2\theta} \tag{1.3.3}$$

There is one drawback and one caveat to calculating the lateral force calibration constant in this manner, however. The caveat is that these equations require only one sloped surface be measured experimentally. The drawback is that the lateral force calibration constant will not be as accurate as using both sloped surfaces. To take both sloped surfaces into account, the following sets of equations can be solved to find a more accurate lateral force calibration constant:

$$p \equiv \frac{W_0'(101)}{W_0'(103)} = \frac{W_{101}'}{W_{103}'} \tag{1.3.4}$$

$$q \equiv \frac{\Delta_0'(103) - \Delta_0'(101)}{W_0'(101)} = \frac{\Delta_{103}' - \Delta_{101}'}{W_{101}'} \tag{1.3.5}$$

$$\alpha \equiv \frac{W_{103}'}{W_0'(103)} \tag{1.3.6}$$

$$\mu_{101} = \frac{-1 + \sqrt{1 + \kappa^2 \sin^2 2\theta_{101}}}{2\kappa \sin^2 \theta_{101}} \tag{1.3.7}$$

$$\kappa = \frac{\mu_{103}}{\cos^2 \theta_{103} - \mu_{103}^2 \sin^2 \theta_{103}} \tag{1.3.8}$$

$$2q = \left(\frac{1}{\mu_{103}} + \mu_{103} \right) \sin 2\theta_{103} \frac{1}{p} - \left(\frac{1}{\mu_{101}} + \mu_{101} \right) \sin 2\theta_{101} \tag{1.3.9}$$

The equations for p and q are number ratios derived from Figure 6 above. Once the values of p and q are known, equation 1.3.7 and 1.3.8 are plugged into equation 1.3.9 to eliminate the coefficient of friction for facet (101). Therefore, the equation can be solved numerically for the coefficient of friction for facet (103). The roots will be selected so that $0 < \mu_{103} < 1$. With this solution, the lateral calibration constant can finally be determined as a function of both slopes:

$$\alpha = \frac{1}{W_0'(103)} \frac{\mu_{103}}{\cos^2 \theta_{103} - \mu_{103}^2 \sin^2 \theta_{103}} \tag{1.3.10}$$

With this “wedge” method of lateral calibration, it is important that each cantilever is calibrated separately due to slight changes in tip radius and also cantilever thickness. Also, the error of the lateral force calibration constant rises rapidly as the coefficient of

friction approaches 1. Ideally, an AFM probe should be selected so that the tip-sample coefficient of friction is less than .7.

Many other lateral calibration techniques would work equally well, and produce accurate results. One such method is the direct application of a known force to the long axis of the cantilever beam[14]. The known force produces a torque in the cantilever which is measured by the change in reflection of the optical beam on the quadrant photodiode. Another technique involves scanning the AFM tip across a substrate that is attached to a spring of known stiffness. As the tip scans across the surface, the spring stretches by a known value. As long as the applied normal force is known, the lateral force calibration constant can be calculated[15-16]. The last technique utilizes a non-contact approach, known as the torsional resonance method. With this approach, the cantilever is oscillated at its resonant frequency. An additional mass is then added to the cantilever, and the change in resonant frequency is measured[17]. The cantilever can even have no additional mass added, with calculations based on the thermally excited resonance and several assumptions (the Sader method)[18]. However, since several of these lateral calibration schemes require specialized equipment and/or specimens, and are not purely in-situ methods, they have not been implemented here. Instead, all lateral calibrations are performed after following the “wedge” calibration method as described above.

1.5 Contact Mechanics and Adhesion

An important design consideration for micro/nano-electromechanical systems (MEMS/NEMS) is the effect of friction and wear on its components. Until now, no MEMS devices employ sliding interfaces due to the detrimental effects of friction and wear[3-5]. As the size of the components approach nanometer length scales, adhesion and

surface forces become dominant and the focus of study for many researchers. Several different models are presented below for this adhesion between materials, including the classic Hertz model, the JKR model, and the DMT model.

In 1882, Heinrich Hertz determined that the contact area between a flat plane of glass and a sphere had a contact area dependent on the load applied, the radius of the sphere, and the Young's moduli and Poisson's ratio for both materials[19]. This model is presented in the equations below, where *a* is the contact radius:

$$a = \left(\frac{PR}{K} \right)^{1/3}$$

$$K = \frac{4}{3} \left(\frac{1-\nu_1^2}{E_1} + \frac{1-\nu_2^2}{E_2} \right)^{-1}$$

where E_1, E_2 are the Young's moduli for the sphere and plate and ν_1, ν_2 are the Poisson ratios for the sphere and plate, respectively. This theory assumes that there are no attractive forces between surfaces and assumes that the contact area of the sphere is much smaller than the radius of the sphere. Although this model is widely implemented for indentation studies, since adhesion is expected at the nanoscale we would anticipate that Hertz contact mechanics are not the most appropriate to consider in this work.

Johnson, Kendall, and Roberts (JKR) proposed a modification to Hertz contact mechanics theory in 1971 to take into consideration the adhesion between two surfaces[20]. The modified equation is presented below:

$$a = \left(\frac{R}{K} \left(P + 3\pi\gamma R + \sqrt{6\pi\gamma RP + (3\pi\gamma R)^2} \right) \right)^{1/3}$$

where γ is the adhesion energy. Several important concepts can be deduced from this equation. First, the contact area is finite with zero applied load. Second, in order to achieve zero contact area, a negative applied load must be added, known as the pull-off force, P_c:

$$P_{c(JKR)} = -\frac{3}{2}\pi\gamma R$$

Derjaguin, Muller, and Toporov (DMT) derived another modification to Hertz contact mechanics in 1975 that assumed the profile of contact remained the same as Hertz, but with a higher overall load due to adhesion[21]. In addition, the adhesion force was not present exclusively while the surfaces were in contact, but also at a finite separation distance. The contact area, a, and pull-off force, P_c, for the DMT model is presented below:

$$a = \left(\frac{R}{K}\left(P + 2\pi\gamma R\right)\right)^{1/3}$$

$$P_{c(DMT)} = -2\gamma\pi R$$

When experimentally acquiring friction or normal force curves as a function of applied load, the DMT and JKR models are applicable to different types of tips and substrates. The DMT model is valid for AFM tips that are very stiff, with very small radii, and weak long-range adhesion forces to the substrate. The JKR model is valid for AFM tips that are very soft, with large radii, and strong short-range adhesion to the substrate. However, most materials do not follow strict JKR or DMT properties; they most often possess a combination of both. For this reason, a non-dimensional physical parameter is used to

quantify the cases in between, known as the transition regime. In 1992, Maugis connected the limits of the JKR and DMT contact parameters for the entire range of possible materials. If the Maugis' transition parameter $\lambda < 0.1$ the DMT model applies. If $\lambda > 5$, the JKR model applies. Any number between .1 and 5 refers to the transition regime. Figure 7 presents friction vs. normal force data for a silicon substrate coated with a thin organic film, and the tip used is silicon with native oxide termination[3]. For reference, the JKR model and DMT model are fit to the same graph. In the DMT model, the friction force is very low just before pull-off because the contact area is very small, and the adhesion at short ranges is weak. In the JKR model, the friction is very high because the contact area is high and the adhesion force is strong just before pull-off. The friction data clearly follows the transition regime adhesion model instead.

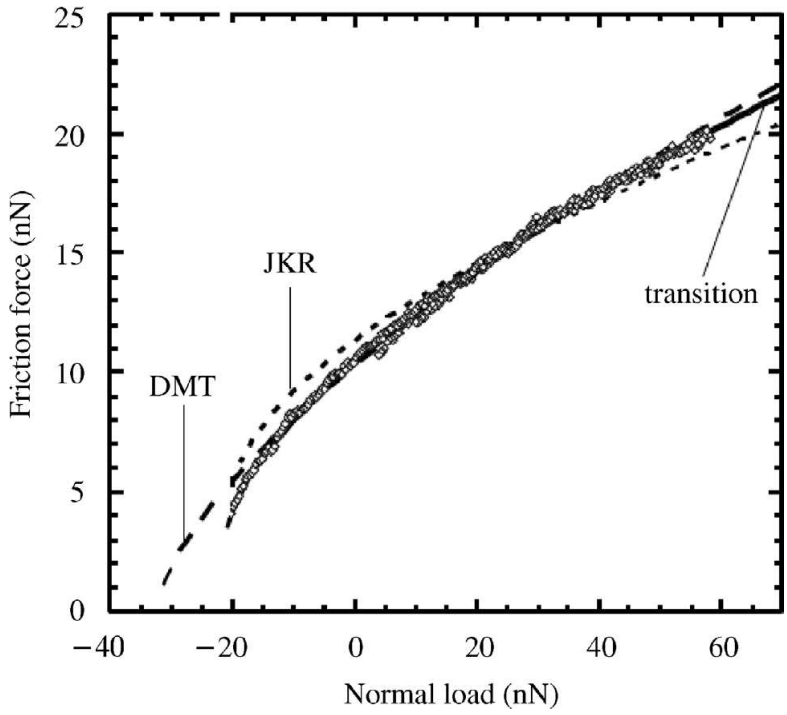

Figure 7: JKR, DMT, and transition regime for a silicon AFM tip with native oxide termination on a silica substrate with a deposition of thin organic film[3].

1.6 Velocity Dependence of Friction

Another important consideration of friction is the dependence of sliding velocity. Many AFM-based studies have been performed to relate the friction force as a function of tip velocity, with ranges from 4-10 nm/s[9, 22-24] up to 200 mm/s with 1-d scanning[6]. It is expected that the velocity dependence will change as all eight orders of magnitude are taken into consideration. The length scales that the velocity dependence has been measured spans from 2 nm scan sizes[9] up to 1 mm[6]. In the earliest work of friction force measurements, Mate et al. reported that there was very little velocity dependence while scanning a tungsten wire across a graphite sample[9]. However, a decade later Bouhacina et al. determined that there was a logarithmic relationship between sliding velocity and friction[22]. The study was performed between grafted layers on silica and a nanotip. The trend in the data can be explained by a thermally-activated Eyring model[25]. Figure 8 presents the force of friction increasing linearly with the logarithm of the tip velocity.

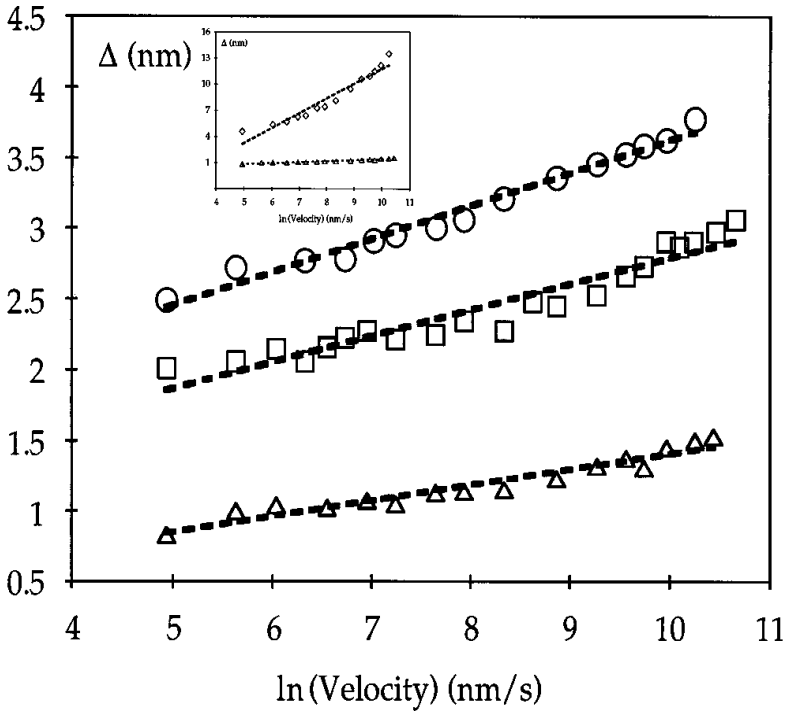

Figure 8: Friction as a function of AFM tip sliding velocity for three different cantilevers. The inset reports data for a fourth cantilever. The substrate was grafted layers on silica[22].

Later work performed in 2000 by Gnecco et al. on NaCl(100) revealed the same linear friction force vs. logarithm of velocity trend as Bouhacina et al. did in 1997. Gnecco et al. proposed that the friction depends on the logarithm of velocity according to a one-dimensional thermally-activated Tomlinson model[24].

Although the derivations of these models are beyond the scope of this work, it is interesting to note that at a critical velocity, the friction force should no longer increase linearly with any further increase in velocity. This critical velocity, υ_c:

$$\upsilon_c = \frac{f_0 k_B T}{k_{eff}^x \lambda}$$

depends on the torsional frequency of the cantilever used for scanning the sample, f_0, Boltzmann's constant, k_B, the absolute temperature, the effective lateral spring

constant, k_{eff}^{x}, and a new constant, λ (not the Maugis parameter). They determined that this critical velocity for a standard cantilever at room temperature is approximately 1.4 µm/s. Previous work performed by Gourdon et al in 1998 fits the thermally-activated Tomlinson model quite well. The scanning was performed with a silicon tip on a thiolipid Langmuir-Blodgett film physisorbed on mica substrates[26]. The scanning velocity range used was between 10 nm/s and 50 µm/s. Changes in scanning velocity were realized by changing the scan size, rather than the scan frequency, which was kept constant at 3 Hz. It was reported that the lateral force signal increased quickly and monotonically with velocity, and then reaches a plateau for all samples scanned. The four samples scanned were a mica substrate, a fluid phase of the Langmuir-Blodgett film, and two scans on solid Langmuir-Blodgett films at different scan angles.

The transition in the slope of the friction force can be attributed to the change from static friction to sliding friction. The tip will stick to the sample as long as the sliding force is less than the static friction force. Once the static friction force is reached, the tip will begin to slide across the sample, and the velocity dependence of friction breaks down. This is presented in Figure 9. For the distinct “arm 4” surface, the transition from static to sliding friction is reached at a critical value of 3.5 µm/s.

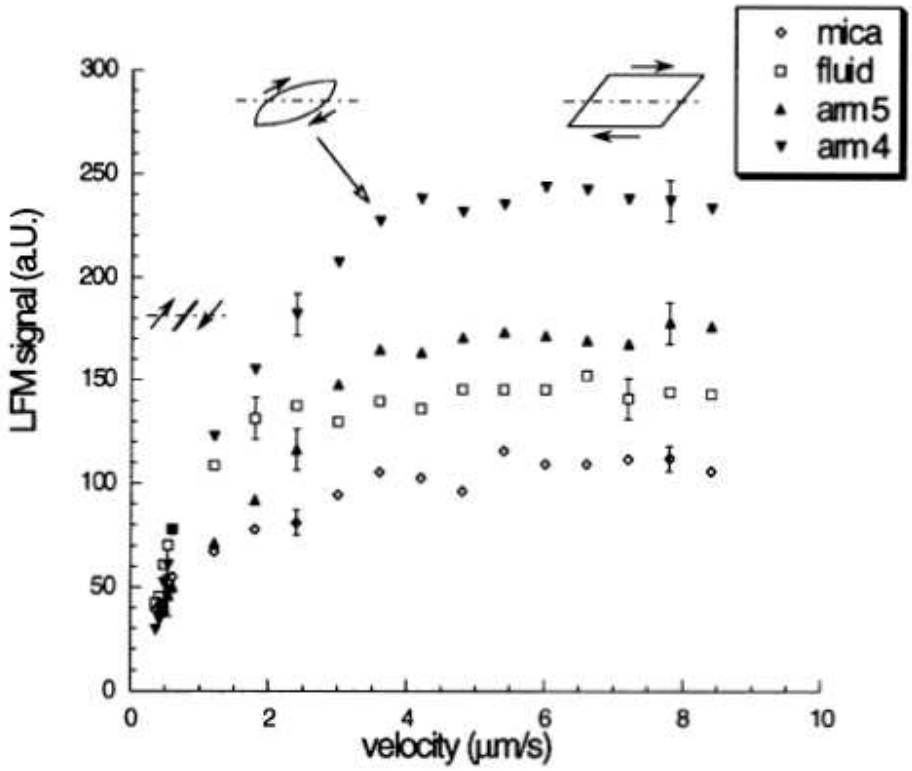

Figure 9: AFM scan with silicon tip on four different substrates[26]. The transition from static friction to sliding friction is reached at approximately 3.5 µm/s for arm 4.

The relation between friction force and velocity discussed until this point has been on the atomic scale, and at relatively low sliding velocities. As the velocity is increased further, to greater than 10 µm/s, new mechanisms arise that cause an increase in the friction force. One such study had been performed by Zworner et al in 1997, which investigated the velocity dependence of friction forces on several different carbon substrates, and at varying sliding velocities[23]. A model has also been presented to account for the experimental friction data at high scanning velocities. Three carbon samples (amorphous carbon, diamond, and highly oriented pyrolitic graphite) were scanned at a range of scanning velocities from 10 nm/s to a maximum of 25 µm/s. For this range, the friction force remained constant, except at very low scanning velocities, which agrees with the

thermally-induced Eyring and Tomlinson models of static friction. Figure 10 presents the friction force as a function of sliding velocity for the carbon-based substrates.

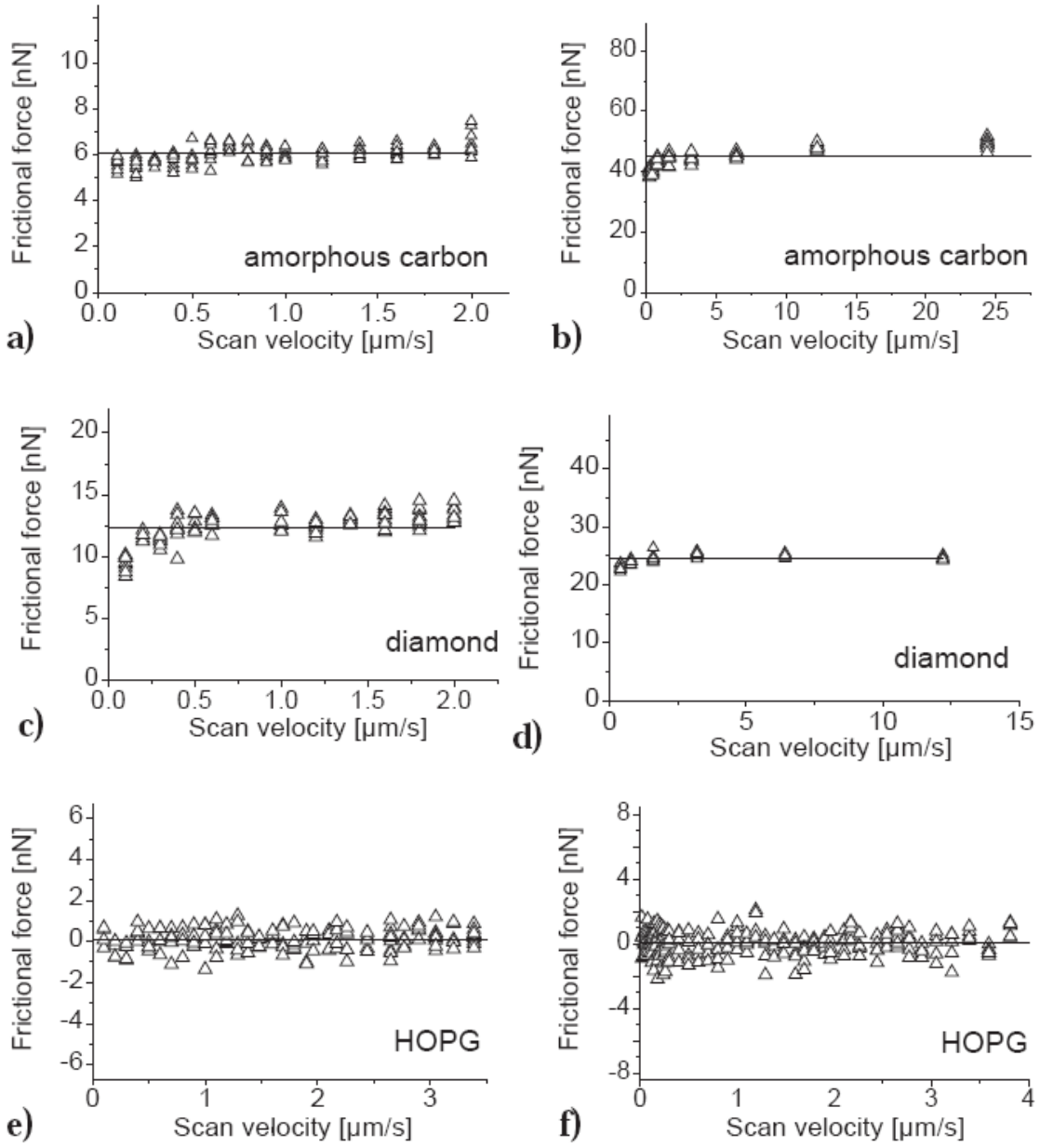

Figure 10: Friction vs. velocity dependence on carbon-based substrates. The friction remains constant as the tip slides across the substrate with no stick-slip interaction[23].

Alternatively, as the scan velocity is increased to greater than 100 µm/s, the tip movement is dominated by viscous damping, and the friction force is again proportional to the sliding velocity according to the following equation:

$$F_{fric} = 2\sqrt{k_x / m_x}\upsilon_M$$

where k_x is the lateral spring constant of the cantilever, m_x is the effective mass of the cantilever, and v_M is the scanning velocity. It is necessary to point out that the model proposed by Zworner et al. does not predict the threshold velocity required to achieve viscous damping, but only the rate of increase of the friction based on the type of cantilever used. Therefore, with other cantilevers and substrates the velocity required to reach viscous damping friction forces may be different. Figure 13 presents the viscous damping effect according to Zworner. In 2002, Prioli et al. performed experiments on boric acid crystals that similarly displayed viscous damping forces at velocities higher than 2 µm/s[27].

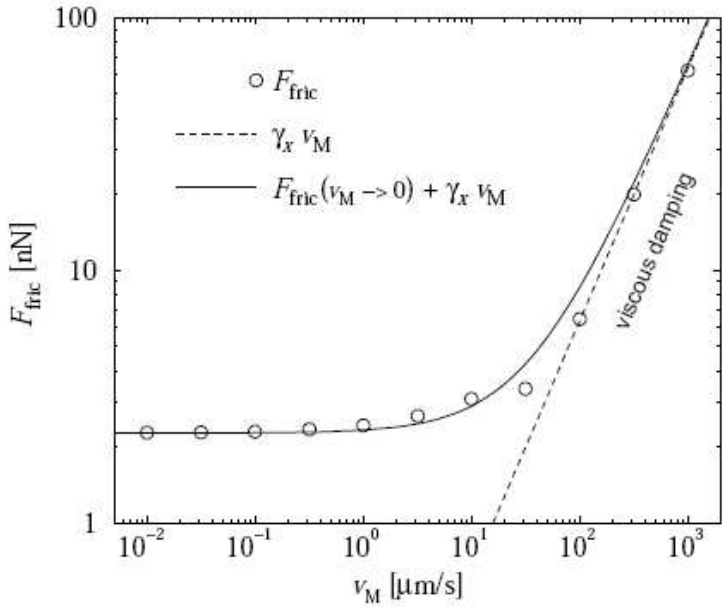

Figure 11: Effect of viscous damping as the sliding velocity between AFM tip and substrate is increased. The substrate is undefined[23].

1.7 High Speed Lateral Force Microscopy

As the velocities of typical MEMS devices approach the meter per second range, it becomes relevant to investigate the nanotribology at these ultra-high velocities. Various systems have been introduced to attain higher velocities, which are typically modifications to existing AFM hardware. In 2005, Tambe and Bhushan developed a system that achieved sliding velocities between 1 µm/s and 10 mm/s with 1-d capability[28-29]. In this system, samples were mounted on a custom calibrated shear wave transducer with its polarization perpendicular to the longitudinal axis of the cantilever. Scanning frequencies ranged from .1 to 250 Hz, and the scan lengths chosen were 2 or 25 µm. A custom data acquisition card was used to process lateral signals at a rate of 25,000 samples per second. One year later, Zhenhua and Bhushan developed another system which has the capability to investigate friction forces at scan rates up to 200 mm/s[6]. In this system, the piezoelectric actuators used in the typical AFM for x and

y direction scanning were replaced with a custom-calibrated ultrahigh velocity stage driven by a piezo-actuator and feedback control using proportional-integral-derivative (PID) algorithms. This system, however, is only capable of scanning along one dimension. Scan lengths chosen were between 25 µm and 1 mm. Lateral signals were processed at rates of up to 80,000 samples per second. Figure 12 presents the friction force versus scanning velocity for the high velocity stage developed in 2005, and the ultrahigh velocity stage developed in 2006. The friction force shows a linear relationship with the logarithmic increase in scan velocity, until very high speeds have been achieved (over 100 mm/s) where the friction increases linearly as a function of scan velocity.

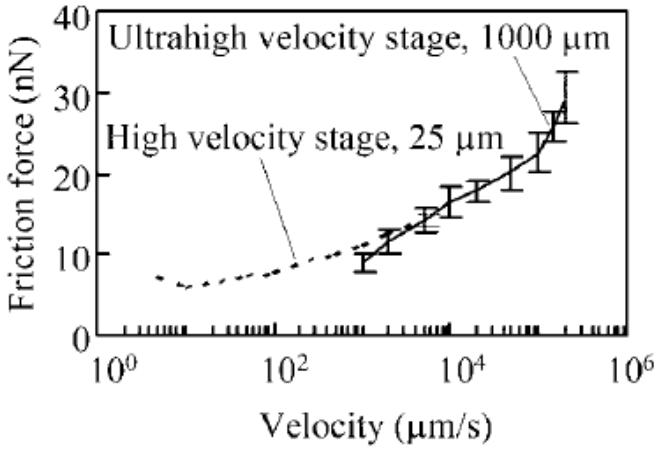

Figure 12: Friction force vs. scanning velocity for Si (100) with native SiO_2. Two high velocity stages were used. The high velocity stage is capable of scanning up to 10 mm/s. The ultra-high velocity stage is capable of scanning up to 200 mm/s[6].

1.8 High Speed Limitations of AFM

In order to increase scanning velocity, two parameters can be adjusted, either the scanning frequency or the scanning length. However, there are limitations to both of these quantities. In terms of scan dimensions, traditional AFM systems are limited in maximum scan length by stage actuators with an upper limit of anywhere between 2 and 100 µm. Piezoactuators can also be limited by non-linear hysteresis effects[30-32]. This

means the voltage required to move the piezo a given distance is not constant over the entire range of piezo motion, causing a loss of spatial precision. At high speeds, creep effects begin to manifest as time progresses as well. As voltage is applied to the piezoactuator, over time the piezo will drift in absolute position. This will also result in a loss of spatial precision, though is more of a problem for maintaining an exact scanned region as opposed to errors in scan velocities.

With respect to adjusting the scanning frequency, the outcome also depends on several factors involving piezoactuator response and system design. The main challenge is that as the scanning frequency is increased, it approaches or even goes beyond the resonant frequency of the piezoactuator itself. This will induce amplitude variations in the actual stage motion as compared to the reference signal (expected motion), which will lead to scan lengths much higher or much lower than anticipated. Phase lag or lead also occurs on either side of a resonance, creating problems with synchronizing the extreme left and right edges of the scanned lines. All of these limitations are of great practical concern when increasing scan velocity; similar challenges and solutions related to the current work will be covered in more detail in Chapter 2.

Finally, in addition to piezoactuator limitations, data acquisition systems are of concern. A typical friction image in two dimensions on the AFM consists of 256 pixels per line, with 256 lines of data. If a line scan frequency of 1000 Hz is desired, the data acquisition card would need to collect 512,000 samples per second. This is higher than the capability of standard data acquisition systems included in most AFM systems. Therefore, specialized hardware is required. Limitations and solutions with data acquisition for current the work will also be discussed in detail in Chapter 2.

Chapter 2: Materials and Methods

2.1 AFM and External Hardware

The AFM used to complete the experiments was an Asylum Research Cypher AFM, with Igor Pro software version 6.22A, and plug-in MFP-3D version 101010+1202. All experiments are performed at room temperature, and the scanning unit is housed within an enclosure that isolates the imaging portion of the microscope from acoustic noise. In addition, the enclosure provides thermal isolation from the surroundings. The piezoactuator scanners on the Cypher system have a maximum range in the X, Y directions of 30 µm scan and a 5 µm scan range in the Z direction.

Two cantilever types were used in the experiments. The first is a diamond coated silicon probe from Nanosensors, type CDT-FMR-8, with an advertised tip length of 10-15 µm, resonant frequency of 60-100 kHz, cantilever length of 225 ± 5 µm, and spring constant of 1.2 – 5.5 N/m. The second cantilever used was a Tetra-17 SiN, with a p-type boron doped silicon probe, cantilever length 450 ± 5 µm, resonant frequency 7-24 kHz, and force constant of .02 - .75 N/m. The tip length is 18 ± 3 µm, and radius of less than 10 nm. The data acquisition rate of the Cypher system is only 50 kS/s, so any experiments performed faster than approximately 80 Hz per line are conducted with the aid of external hardware, especially data acquisition. The external hardware employed is a National Instruments PXIe-1062Q chassis, with a PXIe-6124, 4 channel, 16 bit, 4 MS/s data acquisition card (DAQ). Also included within the chassis is a PXI-5421 arbitrary waveform generator (AWG) capable of outputting at a rate of 100 MS/s and with 16 bit resolution. When high speed scanning is required, the AWG is used to drive the X and Y

piezoactuators, and any signals output from the AFM are acquired by the DAQ. Both the signals output from the AWG and the signals input to the DAQ are timed with an 80 MHz synchronizing clock built into the hardware. Software written within National Instruments LabVIEW programming language was used to control the external hardware for data acquisition, primarily coded by Dr. Sungjun Lee, previous postdoc in the nmLabs. Some modifications have also been made to achieve the results presented here.

2.2 Normal and Lateral Calibration

As described by Ogletree et al in 1996 and in Chapter 1 of this thesis, in order to produce repeatable and quantitative friction force measurements, a normal and lateral force calibration has to be performed for each cantilever used[12]. In both normal and lateral scanning modes, the relative force is displayed as a voltage output from the relevant portions of a quadrant photodiode. Force calibration therefore provides a method to convert output voltage into output Newtons. Prior to performing any lateral calibrations, the normal sensitivity, S_z, must be calculated. The normal sensitivity is the product of two experimentally determined factors on the AFM. The first, called the deflection inverse optical lever sensitivity (Deflection InVOLS) is the sensitivity of the quadrant photodiode and cantilever combination. This sensitivity is determined by taking a force vs. distance measurement, or “force curve”. To begin this process, the overhead optics are used to locate the cantilever, in this case we will perform a force calibration on the CDT-FMR-8 diamond coated probe. The laser is then positioned on the back of the cantilever to maximize the signal entering the photodiode. The position of the laser spot on the quadrant photodiode is centered so that the lateral signal and deflection signal are zero. While the AFM probe is far from the surface, the z-piezo is then fully extended and

retracted, and the deflection signal is recorded. Any slope is known as the virtual deflection of the cantilever and should be set to zero, as the cantilever deflection does not practically change when far from the surface. Figure 13 presents an example of the virtual deflection signal for the diamond coated probe, a minimal error for this instrument, but often much more substantial unless corrected as described.

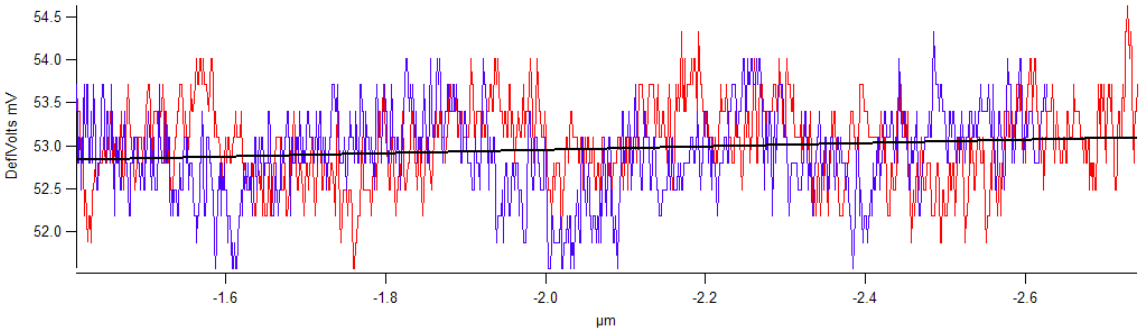

Figure 13: Virtual deflection signal for a CDT-FMR-8 diamond coated probe. The slope of the virtual deflection signal is set to zero for accurate force curve measurements

Once the slope of the virtual deflection is set to zero (essentially subtracted from all F-d curves from that point on), a force curve approaching and contacting the surface is acquired. A force curve taken for the diamond coated probe is presented in Figure 14.

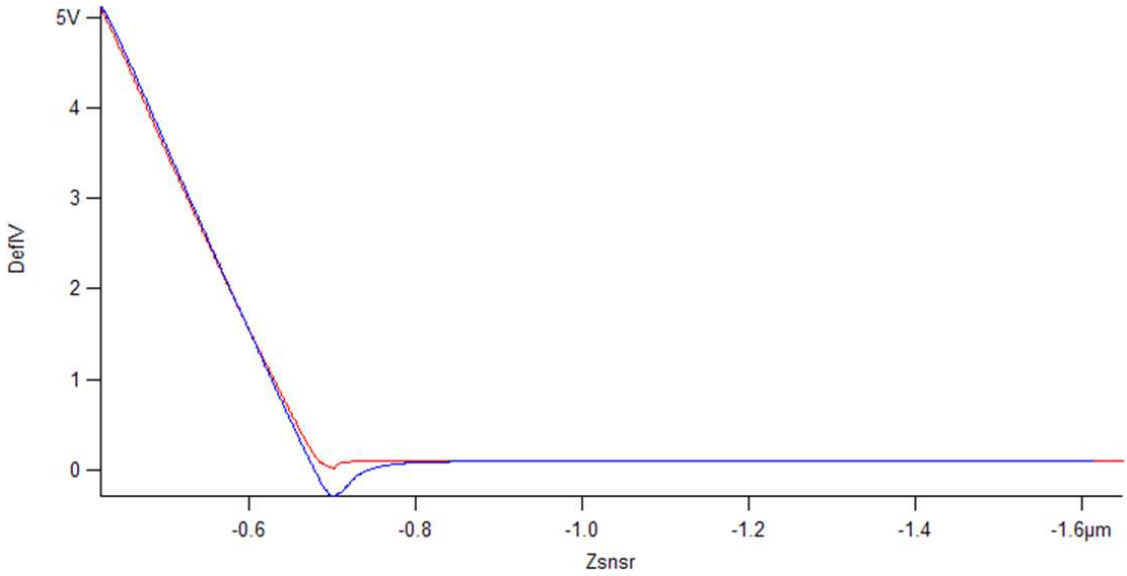

Figure 14: Force curve measured to determine deflection InVOLS for CDT-FMR-8 diamond coated probe. The red and blue lines are the motion of the AFM tip towards and away from the surface, respectively. The slope of the repulsive regime of is the deflection InVOLS.

The red line represents the force collected as the tip approaches the surface, and the blue line indicates the force collected as the tip retracts from the surface. The slope of this line when in contact (the left side of the plot) is known as the deflection InVOLS, and a typical value for the diamond coated probe is between 47 – 50 V nm/V. Once the deflection InVOLS is calibrated, the spring constant k_z is calculated by oscillating the cantilever above the surface, and determining its resonant frequency based on thermal excitations alone. The graph acquired is fit to the simple harmonic oscillator equation, which is a standard function built into the AFM software known as “SHO fit” to the “thermal tune” data. An example of the thermal tune is presented in Figure 15.

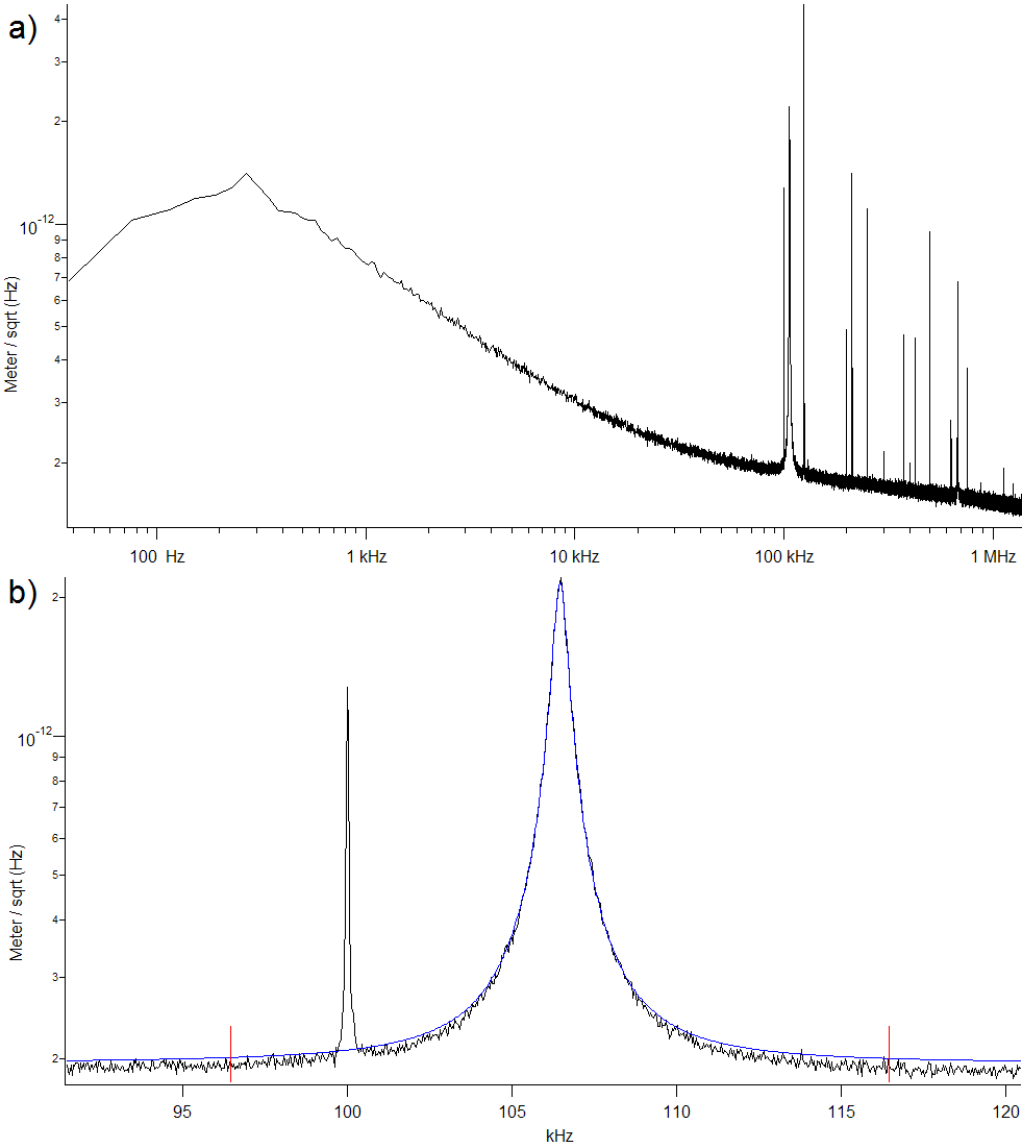

Figure 15: Thermal tune to determine spring constant. a) raw thermal tune collected and b) magnified resonant frequency used for simple harmonic oscillator equation.

Typical values of the spring constant for the diamond coated probe are between 5.5 – 6.2 N/m. Now that the deflection InVOLS, D_z, and spring constant, k_z, is known, the normal sensitivity, S_z, is calculated by taking the product of these two values as shown:

$$S_z = D_z \times k_z = \frac{nm}{V} \times \frac{nN}{nm} = \frac{nN}{V}$$

The normal sensitivity calculated for the diamond coated probe ranges from 250 - 295 nN/V. The normal sensitivity calculated for the SiN probe ranges from 25 - 72 nN/V.

Once the normal sensitivity is calculated for each type of cantilever, the lateral sensitivity, S_x, can be calculated by the "wedge" method developed by Ogletree et al. in 1996, which was described in detail in **Chapter 1.4: Lateral Calibration**. The wedge method is performed by scanning perpendicular to the long axis of the cantilever. The substrate used is a TGG01 characterization grating provided by Micromasch. The TGG01 is a 1-D array of triangular steps having precise linear and angular dimensions defined by the crystallography of the silicon (111) plane[33]. The height of each triangular step is 1.8 µm, and the distance between each peak is 3 µm. The angle of each face is approximately 55º from the surface normal. An SEM and AFM image of the TGG01 grating is presented in Figure 16.

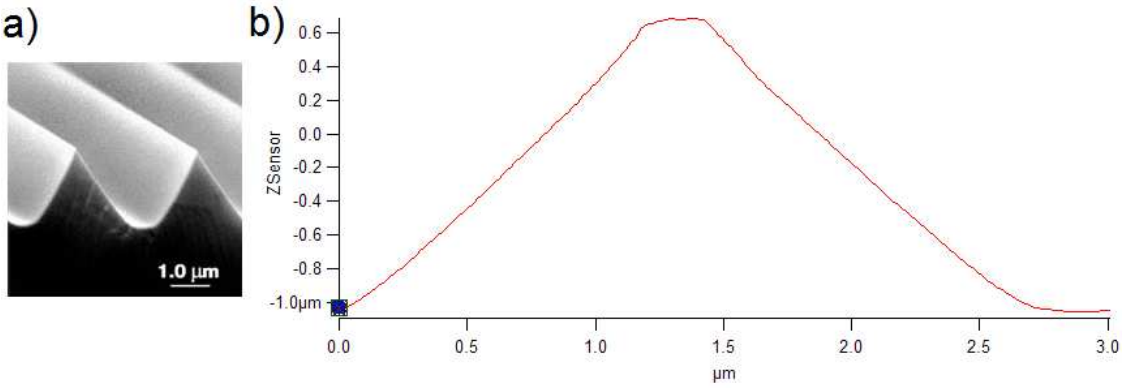

Figure 16: a) SEM Image[33] and b) AFM image of TGG01 characterization grating

The TGG01 characterization grating is scanned with a 3 x 3 µm image, with 256 pixels and 256 scan lines. A program provided by Jason Bemis at Asylum Research is used to increase the normal force by a defined increment for each scan line. The vertical feedback loop, or "Integral Gain", is then set to a relatively high value so that the deflection signal is maintained at a uniform value for each scan line ('constant force').

Slow scan speeds of only 1 Hz are also used to optimize topographic tracking. This is important because if the deflection signal varies appreciably for each scan line, the lateral calibration constants will be less accurate. The lateral signal is recorded for the left-to-right (trace) and right-to-left (retrace) scan directions to create 'friction loops.' The experimentally determined friction loop half-width, W_0, and friction loop offset, Δ_0, for each slope of the TGG01 characterization grating are plotted versus normal deflection signal. Figure 17 presents the friction loop half-width and friction loop offset for the diamond coated probe.

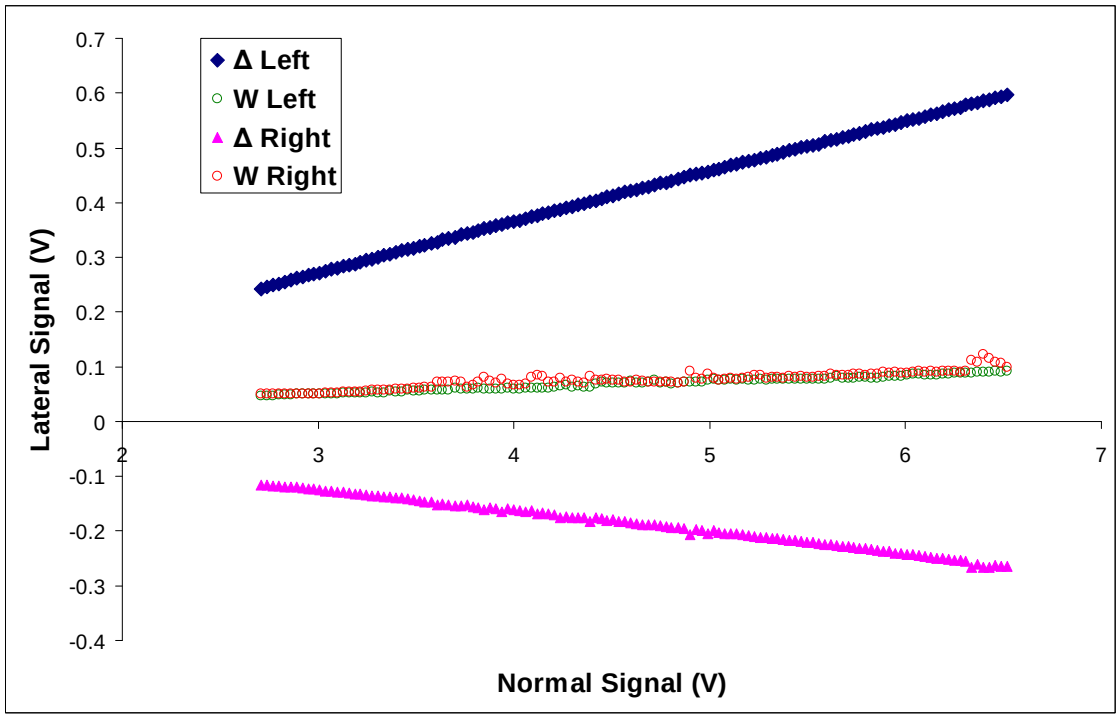

Figure 17: Experimentally determined values of W_0 and Δ_0 are collected by scanning across the TGG01 characterization grating at varying deflection normal loads. The slopes of these lines are used to calculate the lateral force calibration constant for each cantilever desired.

A linear fit is then applied to each of the four data sets. The slope of each line represents the change in friction with normal force for left and right facets, $W_0' = \partial W_0 / \partial L_0$, and the change in friction offset with normal force for left and right facets, $\Delta_0' = \partial \Delta_0 / \partial L_0$. Next,

the angle of each facet of the TGG01 grating must be calculated. This is calculated by a function within the AFM software. Two cursors are placed on the topography graph, and the angle is calculated between the cursors and the surface normal. The angle of the left facet is 55.8º, and the angle of the right facet is 53.2º. These angles will depend on how flat the grating is positioned in the AFM. In the appendix of their lateral calibration paper, Ogletree et al. have provided a method to ensure that the sample is flat[12]. Once the W_0', Δ_0', and angles for each facet are calculated, they can be used to solve equations 1.3.4 – 1.3.10. The lateral sensitivities for the diamond coated and SiN probes are calculated in this manner to be 4280 nN/V and 565 nN/V, respectively.

2.3 High Speed Sinusoidal Scanning

In most AFM scanning systems, each line scan is performed with a constant velocity for each data point. This is accomplished by applying a triangle wave to the piezoactuators. One facet of the triangle wave causes the left-to-right motion of the sample, and the other facet generates the right-to-left motion of the sample. As the scan frequency and scan size are increased dramatically, the piezoactuators are affected by three factors described in detail in **Chapter 1.8**: non-linear hysteresis, creep, and resonant frequency induced vibration effects. When the direction of the line scan switches from trace to retrace, or from retrace to trace, this transition is very sharp when a triangle wave is applied. Such sharp transitions are taxing on the piezo, difficult to reproduce at high speeds due to the limited bandwidth of system op-amplifiers, and excite a range of system references since abrupt steps comprise frequency components for a wide range of harmonics. As a result, the AFM system will begin to “chatter”, or vibrate at certain preferred resonant frequencies. At this point, the vertical feedback, spatial orientation, friction, or

topographic data can become unreliable. To minimize these effects, the top and bottom of the triangle wave is “rounded” so that the transition from trace-retrace is more gradual. To take this idea one step further, the ideal rounding would span the entire line scan, i.e. a sinusoidal wave would be applied to the fast scan axis of the piezoactuator instead of a triangular wave.

There are several advantages to the application of the sinusoidal wave to the fast scan axis. The most obvious is the allowance to scan at higher rates due to decreased acceleration induced vibration of the piezoactuator at line scan edges. Another benefit is that for a given scan size and frequency, the velocity in the center of a line scan is higher than the corresponding triangle wave scan size and scan frequency. This effect is presented in Figure 18. The upper graph represents the triangle wave and sinusoidal waves output from the fast scan axis sensor, which is an external sensor to verify the absolute position of the piezoactuator. The amplitude for each wave will result in a 1 µm travel for the fast scan axis piezoactuator. Since the line scan frequency for this example is 16 Hz, we would expect a 32 µm/s scan velocity for the triangle wave. This velocity is confirmed for the triangle wave in the lower graph.

The sinusoidal wave, on the other hand, generates a maximum velocity approximately 60% higher than the triangle wave. In addition, sinusoidal excitation causes different scan velocities for each pixel in the line scan. This is displayed in the lower graph of Figure 18. From pixel 1 to pixel 125, the velocity increases from 0 µm/s to 51 µm/s. From pixel 126 to pixel 250, the velocity decreases from 51 µm/s back to 0 µm/s. Therefore, for an image consisting of 250 pixels, there will be approximately 125 different velocities employed, with 2 data points for each velocity.

This obviously complicates feature mapping, since standard images present evenly spaced pixels which are recorded at evenly separated time intervals; whereas with sinusoidal scanning, interpolation and/or oversampling is necessary to create a conventional image from the unevenly spaced raw data. Nevertheless, the varying and enhanced velocity which occurs with sinusoidal scanning also provides opportunities, primarily by allowing friction to be investigated over a broader range of, and much higher, speeds before system resonances are excited and degrade the data.

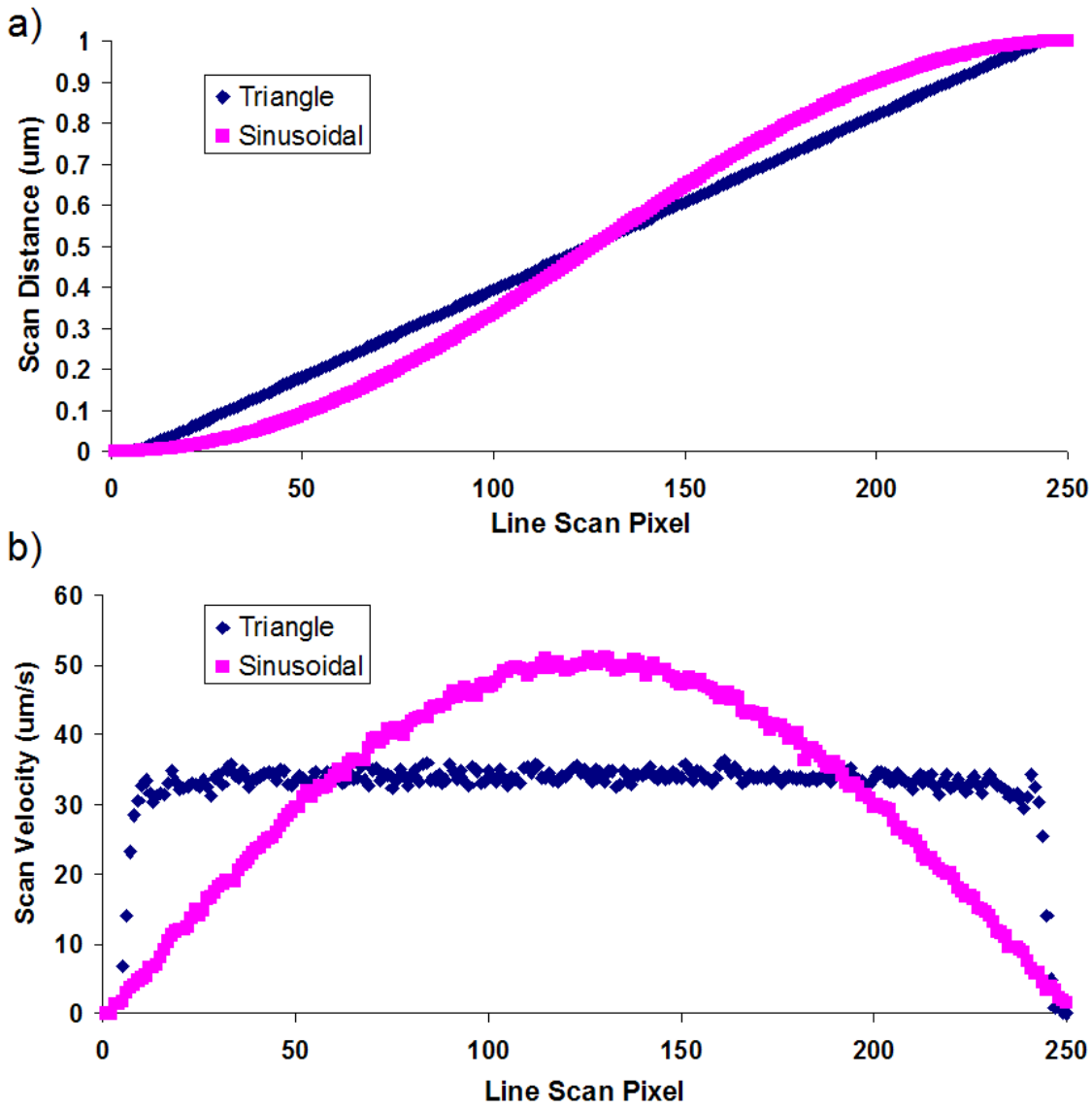

Figure 18: a) Triangle and sinusoidal wave input to the fast scan axis of the AFM and b) the corresponding scan velocity for each type of wave. The sinusoidal wave has a 40% higher scan velocity for a given scan size and frequency.

With this in mind, the application of a sinusoidal wave to the fast scan axis can be applied to friction force curve measurements. Traditionally, the measurement begins with a high normal deflection force, and is decreased incrementally until the AFM tip is no longer in contact with the substrate, i.e. until the pull-off force is reached. By applying a sinusoidal

wave instead of a triangle wave during the friction force curve measurements, the tribological properties of a material can be collected at multiple velocities simultaneously, saving time and resources.

The general setup of the AFM and National Instruments LabVIEW hardware first needs to be explained for high speed scanning alone. To begin with, the AFM tip is engaged with the surface, but the piezoactuator motion with the MFP-3D software is not initialized. The tip maintains a constant normal force with the surface through the proportional-integral-derivative (PID) controller feedback loop, i.e. the feedback is engaged. The AFM tip deflection and lateral signals are output from the AFM to the NI PXIe-6124 data acquisition card through the cross-point panel and output channels in the MFP-3D system, and physically through BNC cables. The sinusoidal wave attached to the fast scan axis and the triangle wave attached to the slow scan axis are output from the NI PXI-5421 arbitrary waveform generator, and connected to the AFM hardware through BNC cables and through the cross-point panel input channels. As described previously, for high speeds we cannot assume that the signal applied to the fast scan piezoactuator to move a given distance is precisely equal to the distance it actually moves. For this reason, Asylum Research has a sensor built into the AFM that monitors the position of the piezoactuator. Unfortunately, though, there is no physical channel to output this digital signal. Therefore, the signal is converted from a digital to analog in the AFM software through a custom PID loop provided by Jeff Honeyman and Anil Gannepalli at Asylum Research. In the conversion process, the signal has a low pass filter applied of 100 kHz, which is not able to be bypassed.

Since the fast scan axis sensor is used to calculate actual scan size and actual scan velocities, it is important that the signal then be analyzed properly. At low scan velocities, the low pass filter does not affect the signal quality appreciably. At high scan velocities, the filtering can make calculating actual velocity difficult. Figure 19 presents the scan distance and calculated scan velocity for the fast scan axis sensor after it has gone through filtering. The line scan frequency is 1024 Hz, and the scan length is 1 µm. For this combination of scan parameters, the average scan velocity for the entire line theoretically should therefore be 2048 µm/s. The lower graph of Figure 19 has the same average scan velocity of 2048 µm/s, but with a wild fluctuation due to the digital to analog conversion. The cause for the wild fluctuations can be seen in the upper graph of Figure 19. The position does not change in a continuous fashion, but more of a step-wise fashion. To solve this issue, a sinusoidal wave with the same amplitude and phase is fit to the fast scan axis sensor data. The instantaneous velocity (at each pixel) is then calculated based on the sinusoidal fit.

When converting the voltage output of the fast scan axis sensor to distance in µm, a conversion factor of 0.267 V/µm is used. When converting the voltage input of the arbitrary waveform generator to the fast scan axis piezoactuator, a conversion factor of approximately 0.370 V/µm is used. The voltage input to the piezoactuator is then amplified by 15, for a final conversion factor of 5.545 V/µm.

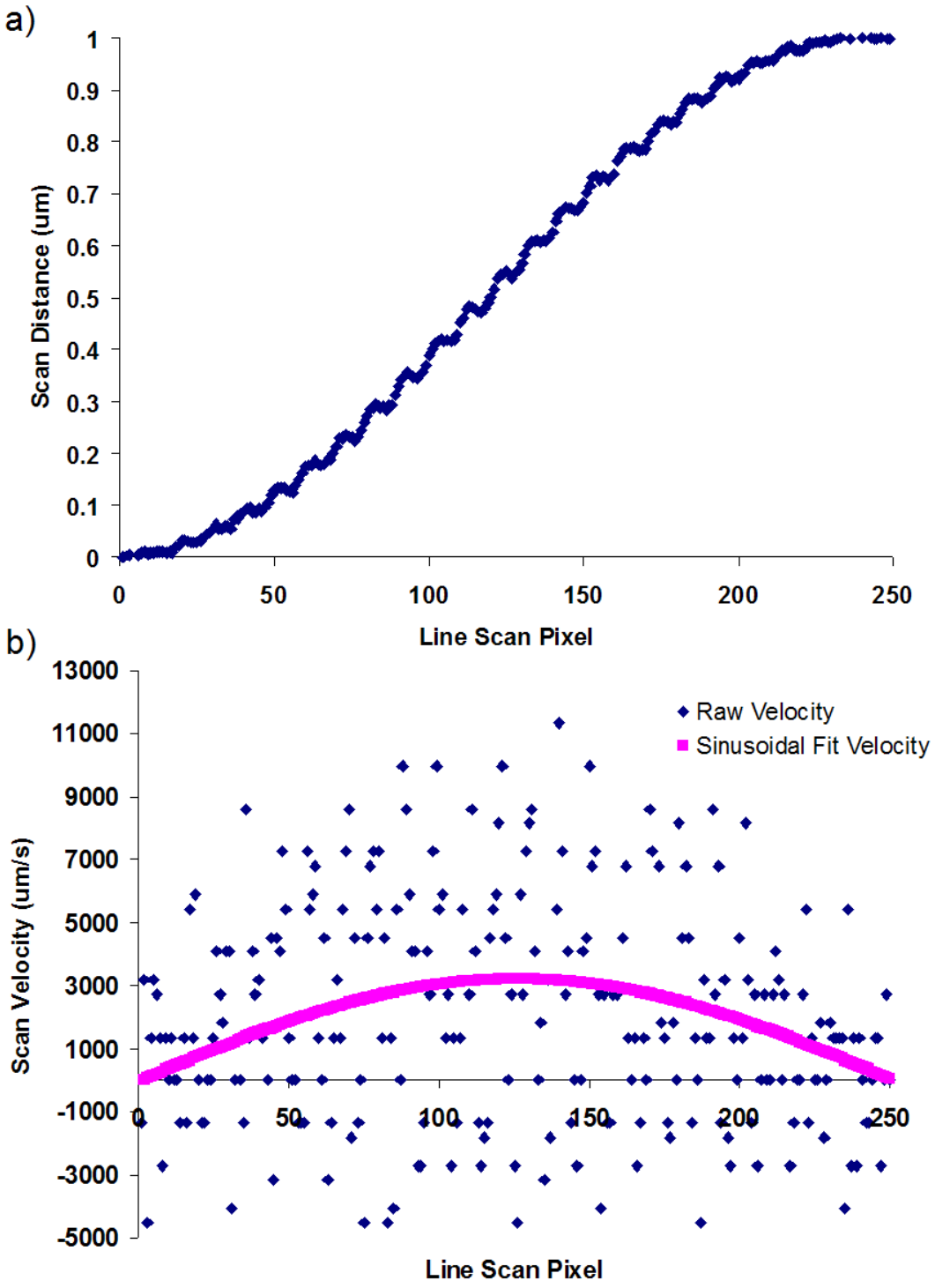

Figure 19: a) Fast scan axis sensor for the AFM, graphing position for each pixel in a line scan. The steps in the signal are due to filtering effects from digital to analog conversion and b) the calculated velocity based on the scan distance is erratic due to the filtering. These effects are corrected by applying a sine wave fit to the graph with the same amplitude and phase.

2.4 Friction Force Curves with Disabled Feedback Loop

Friction force curves are used to gain valuable insight into the tribological properties of materials. The slope of the force curve provides the coefficient of friction, and the pull-off force gives insight into adhesion and contact mechanics. To practically obtain such a friction-force curve, a high deflection normal force of the AFM tip is applied to the substrate. The lateral trace and retrace signals are simultaneously captured to determine the local friction applying the calibration procedures described above. Finally, the normal force is decremented, the lateral signals recorded again, etc. until the tip and sample lose contact (friction goes to zero, often at a negative normal force due to adhesion effects). To obtain the highest resolution, many force intervals must be taken, which can thus require long scanning sessions. A new scanning technique has therefore been developed to reduce the scanning time dramatically for friction force curve investigations, while maintaining force interval resolution.

Although appropriate for imaging at any speed, this method is applicable with high speed imaging, leading to results even faster. The technique involves engaging with the surface, but then turning off the vertical feedback so that a constant force is no longer maintained. The tip is scanned along the surface, and the force between the tip and sample will then vary depending on the surface topography. Figure 20 presents a diagram which is useful for clarifying the technique for friction force curve collection with a disabled feedback loop.

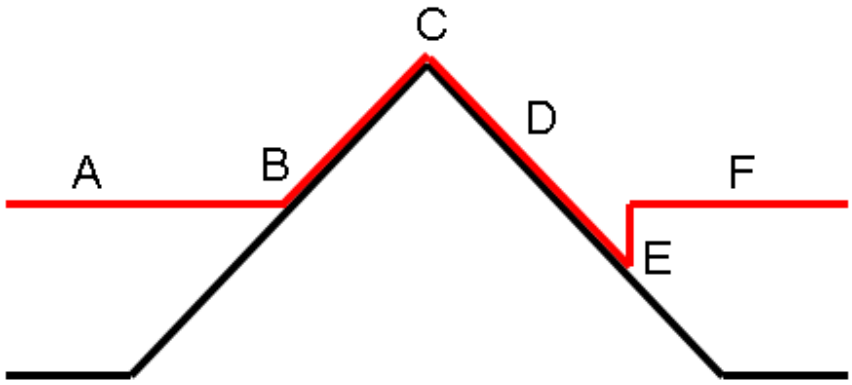

Figure 20: Description of the friction force curve acquisition by disabling the feedback loop. The black line represents the actual topography of a substrate. The red line represents the travel of an AFM tip with the vertical feedback loop disabled. Section A represents non-contact. From section B to C represents the initialization of contact and an increasing deflection (i.e. normal force) as the tip scans over the protrusion. Part C to part D yields a decreasing deflection or normal force. Part E represents the attractive regime of inter-atomic potential and subsequent pull-off force. Part F returns the probe to the non-contact regime.

The black line in Figure 20 represents the actual topography of the sample chosen for friction force curve analysis. The red line represents the AFM tip position as it is scanning across the sample. Let us assume that the AFM tip is scanning from left-to-right, or from position A to position F. At position A, the tip is not in contact with the surface. The deflection at this point is zero, and so there is no normal force or lateral force applied to the sample or AFM tip/cantilever. At point B, the topography of the sample increases enough for the tip to come into contact with the surface. At this position, the normal deflection applied is exactly zero (in the absence of adhesion forces); however, there will be a positive lateral (friction) force present. At point C, the topography has increased to its highest point; here, the deflection normal force and lateral friction force between the tip and sample will reach their maxima. As the topography diminishes, i.e. towards position D, the deflection and lateral forces then decrease. At point E, the force between the tip and sample is attractive, rather than repulsive. The cantilever adheres to the sample until the pull-off force is reached, in which case the tip

and sample no longer remain in contact. At this stage, Point F, the tip and sample are no longer in contact, and the deflection normal force and lateral friction forces are necessarily zero again as with point A.

A TGG01 characterization grating (provided by NT-MDT) was the substrate used to test the technique[33]. Since high scanning velocities are not necessary to verify the effectiveness of this method, the National Instruments equipment was not used for this experiment. Ideally, any sample can also be used with this technique. However, the topography to be characterized, and the type of AFM cantilever selected, will dictate the range of forces applied. Since the TGG01 calibration grating has a topographic difference of 1.8 µm from the top of the triangle to the bottom, a very flexible cantilever was selected for this experiment to avoid fracturing the lever. The SiN Tetra-17 probe (provided by K-Tek Nanotechnology, LLC) was ideal, as the spring constant is on the order of only 0.2 N/m, and the length is approximately 450 µm. Samples with less topographic variations may be similarly characterized, but the selection of the AFM cantilever should be different, e.g. with a higher spring constant in order to maintain an equivalent force range. Samples that are completely flat, i.e. mica or highly oriented pyrolitic graphite, may also be scanned provided that they are mounted at a tilting angle. While scanning the TGG01 characterization grating, practically it does not make much of a difference whether the orientation of the 1-D triangular ridges is perpendicular or parallel to the fast scan axis of the AFM. The only requirement is that the fast scan axis is perpendicular to the long axis of the cantilever as usual, so that lateral forces can be measured with optimal sensitivity.

Once the deflection normal force and lateral friction forces are acquired for an image, they are analyzed computationally with either Microsoft Excel, National Instruments LabVIEW, or MathWorks MATLAB, depending on the dataset, sophistication, and necessary automation requirements. These programs are used to subtract each retrace image from the trace image to obtain friction values in volts. These values are converted to force by the lateral sensitivity calculated in **Chapter 2.2**. Each friction force corresponding to the varied normal deflection forces is recorded, and the friction force curve can finally be extracted for the entire image. Evidently this method works best when specimens are homogenous, though heterogeneous samples can also be analyzed assuming there is a way to identify distinct regions of interest for later calculations based on regions of interest (e.g. using corresponding topographic or phase image contrast).

2.5 High Speed Friction Force Curve Mapping

Friction force curves are traditionally performed on homogenous substrates, on areas where the topography does not influence the desired adhesion characteristics. In fact, the friction signal is typically averaged over an entire scan line or image frame to improve signal to noise resolution, minimize the influence of defects, and provide the mean surface response. However, this makes it impossible to investigate the friction properties of defects, topography, and phase changes, of tremendous relevance for nano- or micro-scale devices. Leveraging high speed imaging for efficient measurements, we therefore propose a friction force curve mapping method to extract friction properties such as the friction at zero force, or the coefficient of friction, with nanoscale spatial resolution. The approach requires a sequence of images for a single area, with each image acquired at a

different setpoint force, and then simply extracts friction-force curves in a pixel by pixel fashion to calculate and map local friction properties.

Of course with patience, this technique can also be implemented using standard speed imaging, requiring no further hardware than an AFM (i.e. high speed data acquisition, and/or shaped actuator waveforms are not necessary).

To demonstrate this principle, friction force curve maps were acquired for a SiO_2 film with microfabricated pits partially filled by thiol-based self-assembled monolayers attached to an underlying Au film, Figure 21. This is a model sample for friction force curve mapping, since it exhibits minimal topographic contrast which can mask friction data, while supplying phase contrast between the two regions when using standard AC-mode AFM. It is therefore straightforward to compare the results from traditional imaging modes with the newly developed quantitative friction mapping technique.

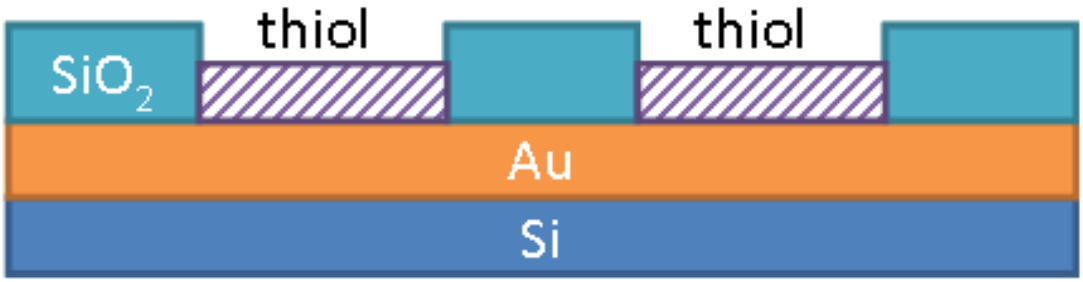

Figure 21: Model specimen for friction force curve mapping, with self assembled monolayers of thiols in microfabricated pits on SiO_2 films.

The specimen was prepared by Andreas Andersen and Duncan Sunderland, iNANO, Aarhus University, using polystyrene spheres as a shadow-mask. The procedure follows, sketched in Figure 22. Briefly, a Si wafer substrate was coated with 30 nanometer of Au. An array of 500 nanometer colloidal silica spheres was then deposited by spin coating. The Au and colloidal silica sphere surface is next coated with a 13 nm thick layer of SiO_2. The silica spheres are finally removed, leaving reasonably ordered ~500 nm pits in

the SiO_2 layer, with Au at their base. A thiol based self-assembled monolayer is then deposited onto the Au surface via dip coating. The thickness of the thiol is between 5-10 nm, leaving a topographic difference between the SiO_2 and thiol surfaces of between 3-8 nm.

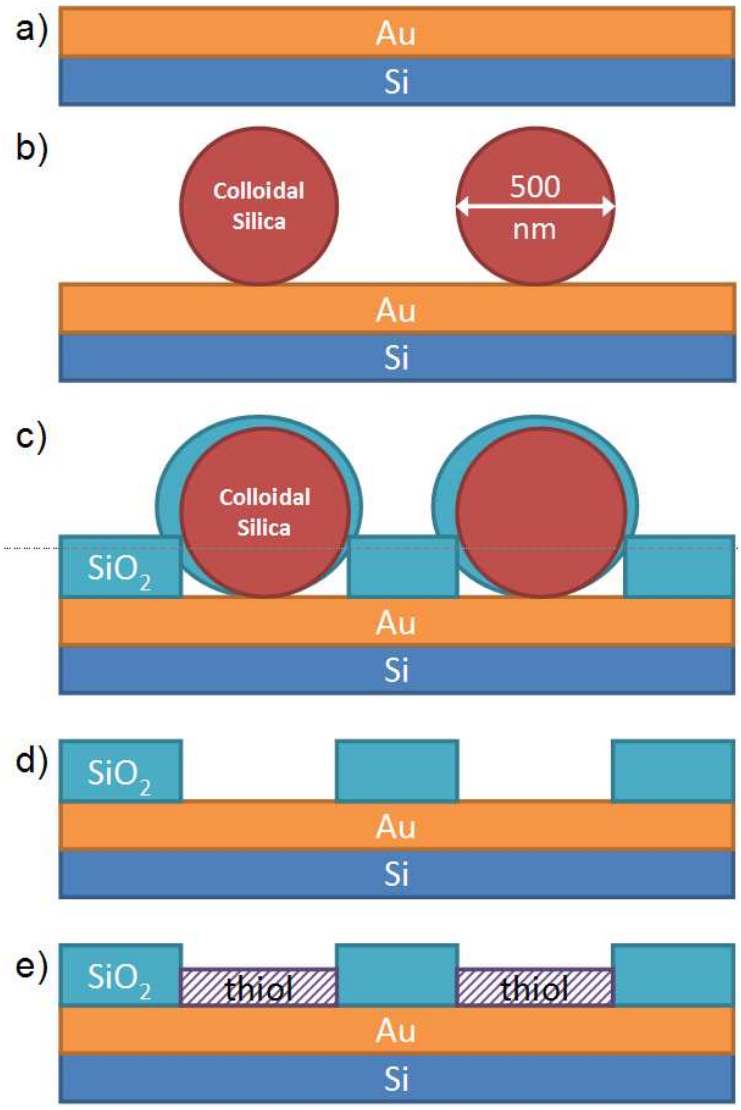

Figure 22: Model fabrication of self assembled monolayers of thiols in microfabricated pits on SiO_2 films. a) Au deposited on Si wafer b) colloidal silica deposited by spin coating c) SiO2 coating applied d) removal of silica spheres e) thiol deposition by dip coating.

The AFM cantilever chosen for the experiments was a CDT-FMR-8 diamond coated probe. The hardware and software setup is the same as described for the high speed

sinusoidal scanning in Chapter 2.3. Since the thiol feature size is approximately 500 nm, a scan size of 1 µm was chosen. Scan frequencies as high as 1000 Hz were used. The tip was engaged with the sample, with a high deflection normal force of 765 nN. The external hardware applied a sinusoidal wave to the fast scan axis of the piezoactuator, and a triangle wave to the slow scan axis of the piezoactuator. Once the 250 x 250 pixel image was completed, the process was then repeated at but with a decremented force. The trace and retrace images for each normal force were then subtracted, and the resulting friction loop width in volts was converted to friction force in nN with the lateral calibration method described in Chapter 2.2. The result is a stack of 28 distinct 250 x 250 pixel friction maps for a sequence of discrete normal forces. For each of the 62,500 pixels, friction force curves are then extracted, a linear fit is applied to determine the friction at zero force, and the slope yields the coefficient of friction over the range of normal loads. The friction at zero force and coefficient of friction values are finally mapped for comparison with topographic or other standard AFM images.

One issue that may require correction when utilizing sequential images as described is specimen drift, especially when slower speeds or large data-sets are employed. This is easily corrected with standard drift correction algorithms using common image processing software, such as Matlab, ImageJ, etc. This pre-aligns features, for example based on simultaneously acquired (and unchanging) topography data, before friction force curves are calculated per pixel. The specific drift correction routine implemented here is a plug-in for ImageJ created by Qingzong Tseng, postdoctoral fellow, European Molecular Biology Laboratory[34].

Chapter 3: Results and Discussion

3.1 High Speed Sinusoidal Scanning

Sinusoidal scanning was performed at high speed with a CDT-FMR-8 diamond coated probe on a cleaved mica substrate. The normal calibration constant for the cantilever was calculated with force curves and thermal tune to 292 nN/V. The lateral calibration constant was calculated with the wedge method to 4280 nN/V. The deflection set-point force applied to start each scan was 3.5 volts, or approximately 1022 nN of force. This normal force was chosen because the feedback loop responsible for maintaining constant force was too slow at very high scan rates, which resulted in normal force variations between 300 nN and 1300 nN. A standard deflection set-point force is typically <1V, or <292 nN for this cantilever, but scanning with this low of a normal force would result in loss of contact with the surface for depressions in the substrate. Conveniently, though, since friction can reasonably be assumed to be linearly proportional to normal force in this loading range, the friction signal at each pixel can be normalized by simply dividing by the normal force at the same location. Taking the corresponding average of each friction image of data, based on a series of images acquired with distinct velocities, yields the average normalized friction versus scan velocity of the diamond probe on mica, Figure 23. The friction increases linearly versus the logarithm of scan velocity at low rates, agreeing with the relationship proposed by Bouhacina et al. for the thermally-activated Eyring model[22]. The data is also in agreement with the 1-D thermally-activated Tomlinson model by Gnecco et al. [24] As the velocity increases, however, the slope of the friction versus scan velocity increases dramatically, a result of viscous

damping forces. This is in agreement with data reported by Prioli et al., [35] as well as Zhenhua et al., [6] and Zworner et al. [23]

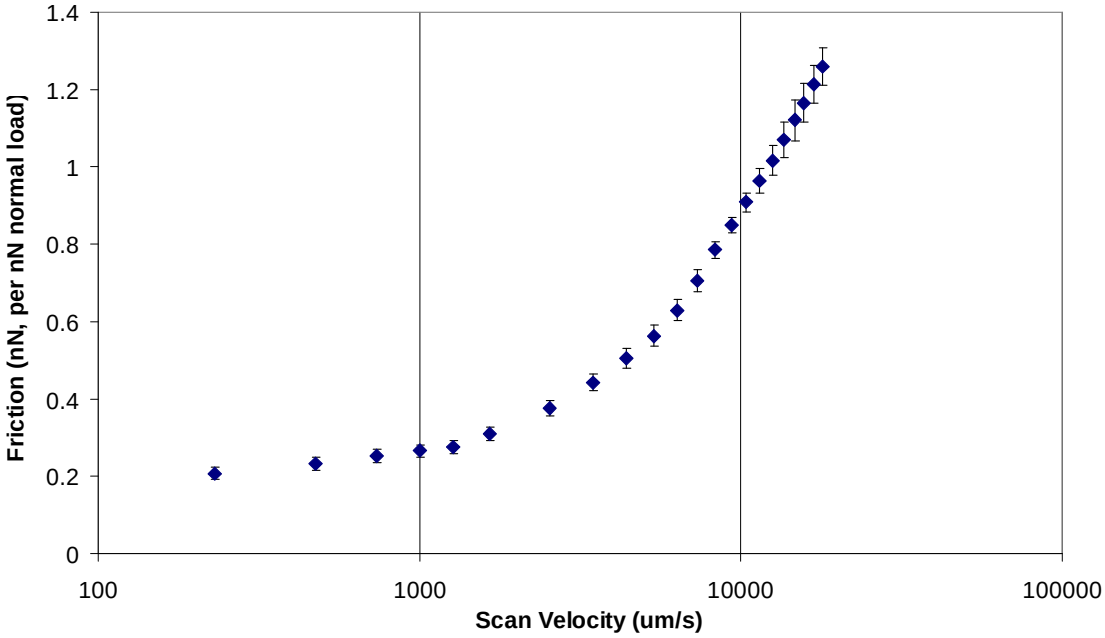

Figure 23: Friction versus scan velocity for a diamond coated probe on cleaved mica substrate.

Notably, for each of the data points in Figure 23, a sinusoidal fast scan axis rate of 1000 Hz was employed. The scan velocity was thus modified by decrementing the scan size, in steps of .5 µm from 9 µm to .5 µm. The points are not evenly spaced since the true distance traveled, and hence velocity, is determined based on the actuator position sensors as described previously.

Although the sinusoidal approach enables variable speed measurements in a single image, this initial experiment only used the top 5 percent of scan velocity data for each friction image (Figure 24), i.e. the middle 50 pixels of each line throughout the 250 line image. Therefore, 12,500 friction data points were averaged in the calculation. The corresponding standard deviation is plotted as the error bars in Figure 23.

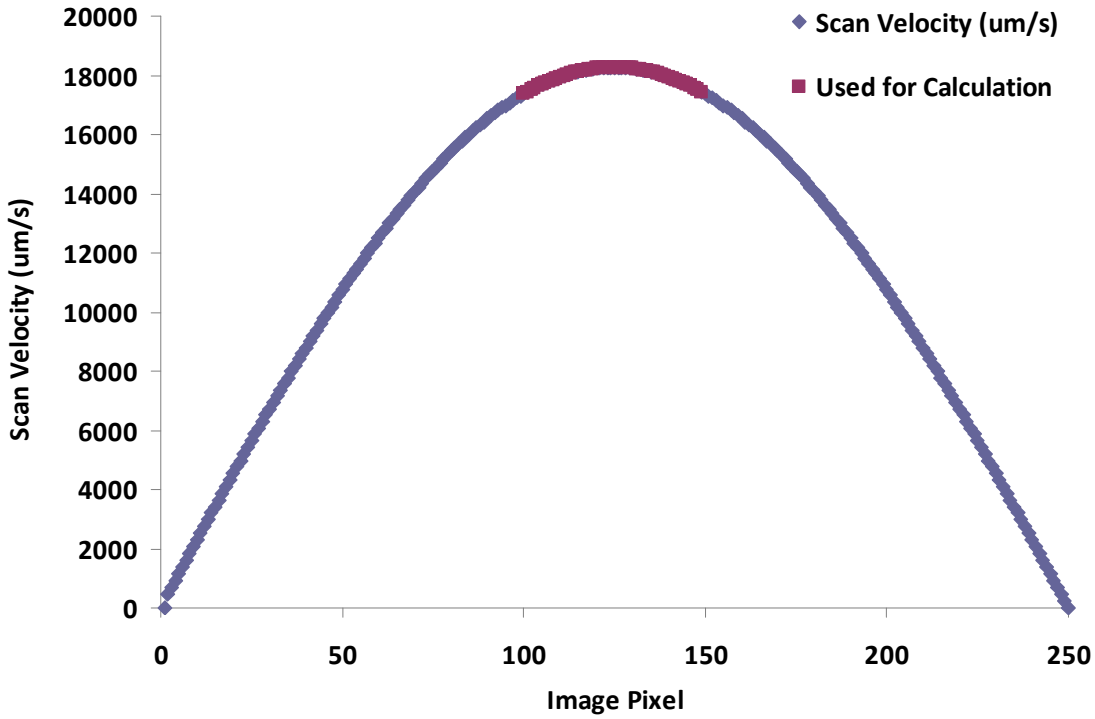

Figure 24: Schematic of the segment of the line scan used for velocity calculation. The center 50 pixels highlighted in purple represents the top 5% of scan velocity per line.

Instead of only using data from a particular velocity (the maximum for Figure 23), the rest of the data from Figure 24 can be used to determine friction vs. a range of velocities. Figure 25 presents the average normalized friction as a function of calculated scan velocity for images scanned over distances of 9 µm, 3.5 µm, and 1 µm as shown. As expected, the range of velocities is different for each of these settings, but several trends are apparent.

First, each of the conditions reveals some hysteresis in the friction values. This is partially due to variations in topography, since the 9 um data incorporates results from a much larger area than the 1 um case. Even more important are acceleration effects, which appear to scale with the maximum velocity (here image size). Basically, the acceleration or deceleration for a sinusoidal based scan is highest at the low velocity locations on each

edge of the friction data, where the transition from trace to retrace occurs as in Figure 24. At these positions in the data (speeds of tip motion), an apparent friction hysteresis results. For Figure 25, this transition occurs at ≈5000 µm/s for the 9 µm maximum scan size, ≈1000 µm/s for the 3.5 µm case, and ≈250 µm/s for the 1 µm data. These results therefore introduce new insight into friction properties under realistic conditions, where velocity and/or acceleration can change, while also allowing traditional friction parameters (acquired with constant velocities) to be compared.

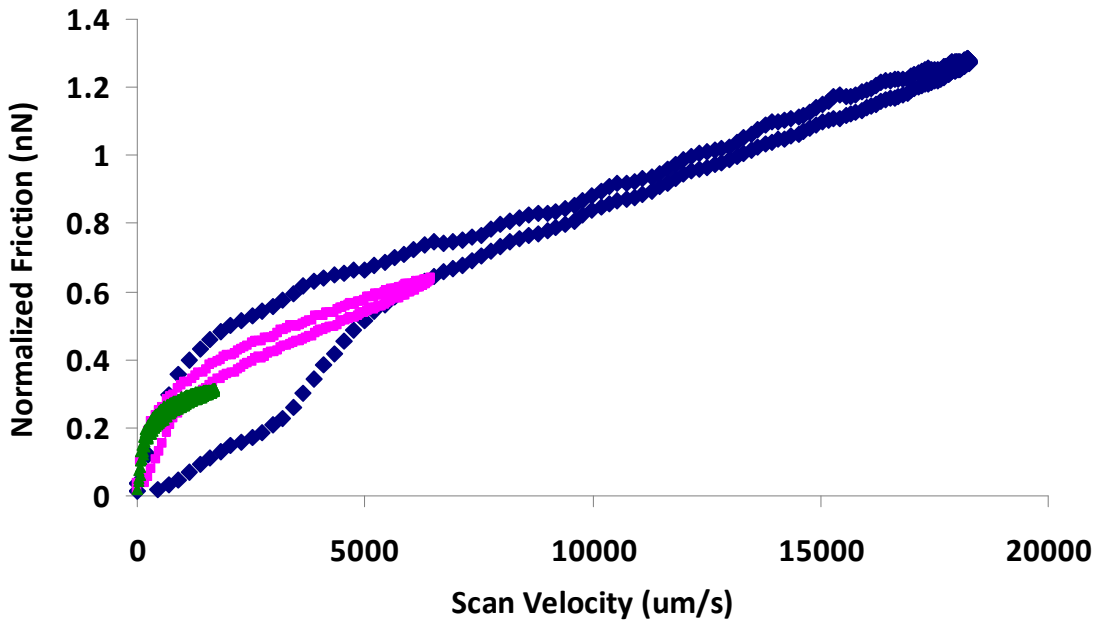

Figure 25: Normalized friction vs. velocity for 1000 Hz. 9 µm scan (blue), 3.5 µm scan (pink), and 1 µm scan (green) on mica with diamond probe.

The application of a sinusoidal wave to the fast scan axis can also be implemented for friction force curve measurements, where sequential images are obtained with decremented forces instead of scan ranges. The same diamond probe and substrate were used, so the normal and lateral calibrations were the same as with the above experiment. A uniform scan size of 1 x 1 µm was employed, at a much slower line scanning

frequency of just 64 Hz (still 64 times faster than standard). The deflection set-point force in volts was then decremented, image by image, in 16 steps from 5 V to -.225 V, equivalent to a range in force of 1512 nN to -32 nN. One set of trace and retrace images were collected for each set-point force. Figure 26 presents the compiled friction force versus scan velocity curves for distinct normal forces. As before, although the target normal force for each set of trace and retrace images is constant, the actually measured normal force (based on the deflection signal) can vary with topography and time, leading to scatter in the results most notably in the 770 nN case.

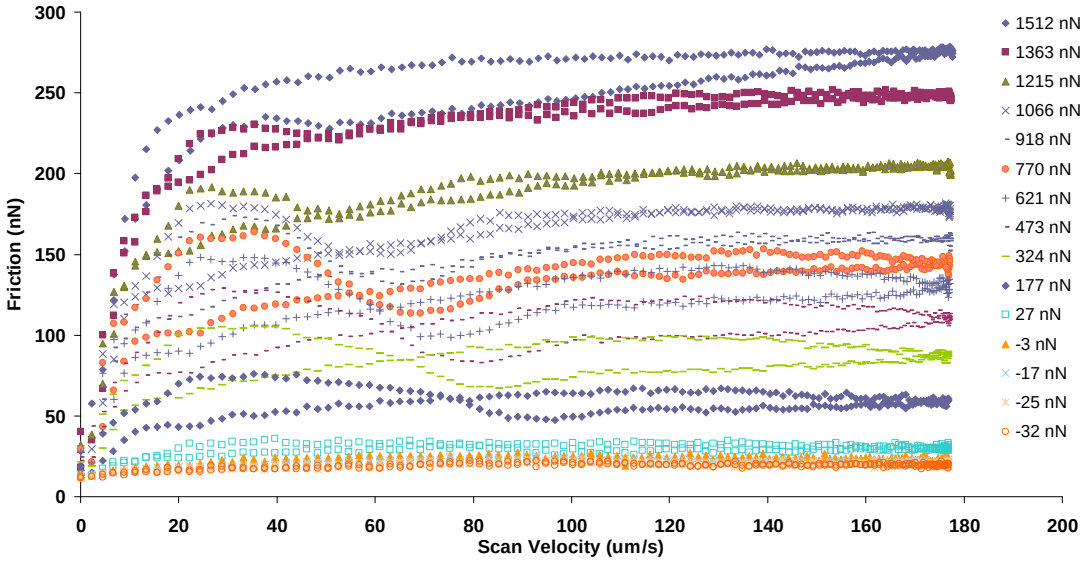

Figure 26: Friction vs. velocity for 64 Hz, 1 µm scan on mica with diamond probe. The deflection normal force is decreased from 5V to -.225 V (1512 nN to -32 nN) to acquire friction force curves at any velocity.

Friction force curves for any given velocity can then easily be extracted from such data by selecting a particular speed and extracting the friction forces as a function of normal force, i.e. simply drawing a vertical line through Figure 26. Figure 27 presents such a friction force curve acquired from the top 10 percent of scan velocities in Figure 26, i.e. scan velocities of 165 µm/s and higher.

The standard deviation of the data is included as error bars. Notably, the normal force was not normalized for this dataset as it was with Figure 23, to evidence the relatively negligible influence of topographic effects, acceleration effects, etc. The coefficient of friction is finally calculated based on the slope of the friction versus normal load, yielding 0.172 ± 0.017. The friction at zero applied force is 30.0 nN ± 14.8 nN.

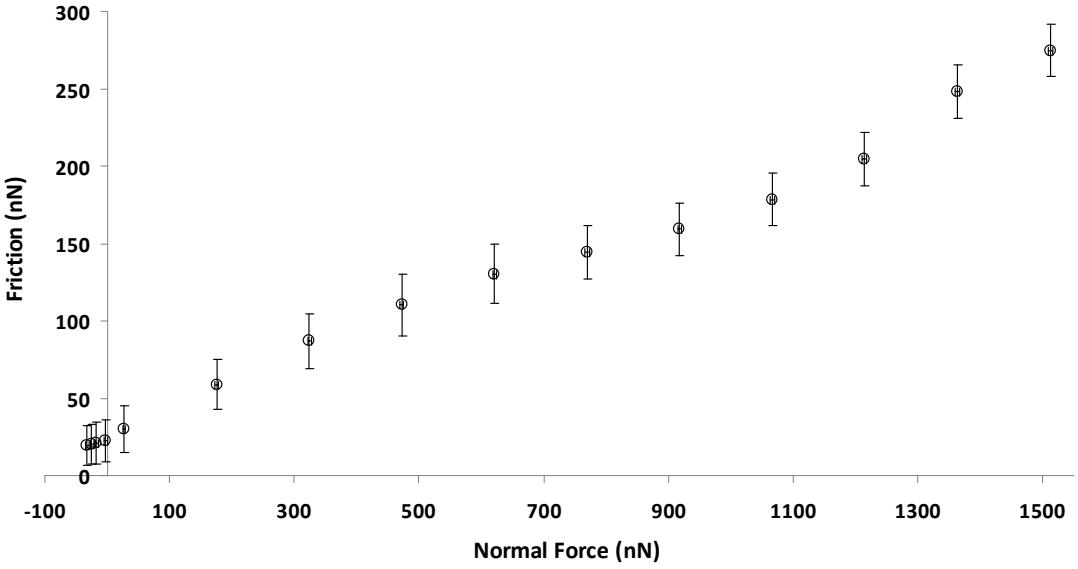

Figure 27: Friction force curve extracted from the top 10% of scan velocities in Figure 26.

An equivalent experiment was performed on an ultra-nano-crystalline-diamond (UNCD) specimen provided by O. Auciello, ADT, Inc. The same scanning parameters and cantilever were used for this experiment as before, except the deflection normal force was not applied in the attractive regime of inter-atomic potential due to much stronger topographic variations than with the mica specimen considered above. The deflection set-point force in volts was decremented by 14 steps from 5 V to 0 V. This corresponds to a force of 1493 nN to 0 nN. Figure 28 presents the resulting friction versus scan velocity for this range of normal forces. Scatter in the data is much more profound, primarily due to the much greater range of topographic features, which can couple into friction signals.

Such topographic effects can be normalized if desired, but the process will require substantial additional calculations and are encouraged as a topic of future work.

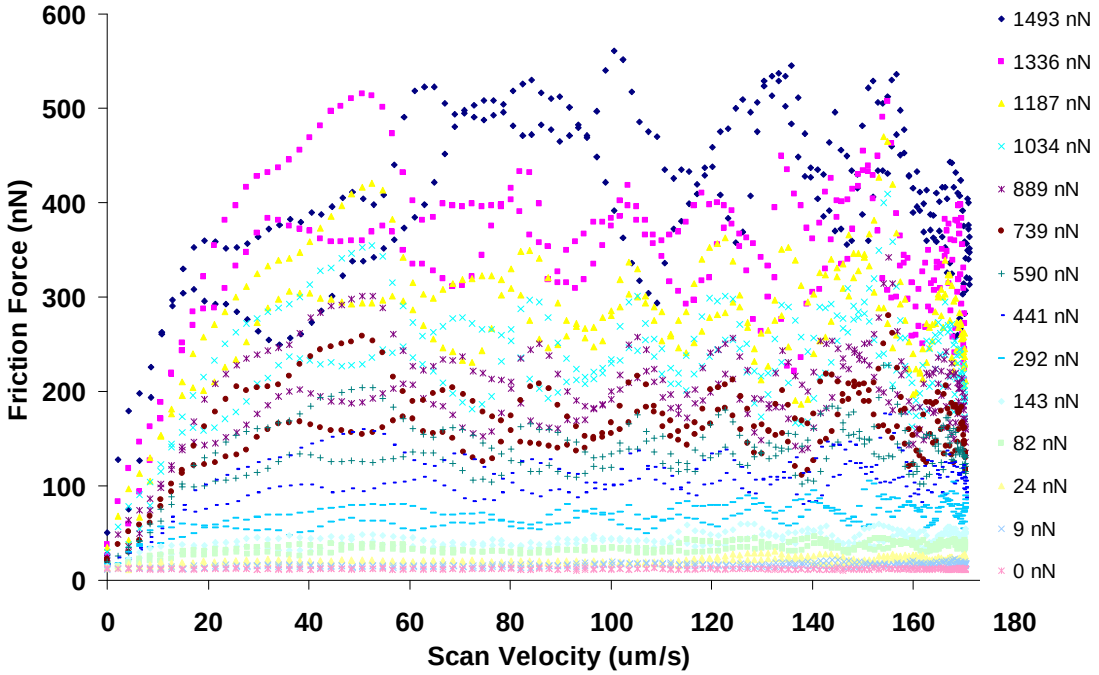

Figure 28: Friction vs. velocity for 64 Hz, 1 µm scan on diamond with diamond probe. The deflection normal force is decreased from 5V to 0 V (1493 nN to 0 nN) to acquire friction force curves at any velocity.

Figure 29 presents the friction force curve taken from the top 10 percent of scan velocities in Figure 28, i.e. scan velocities of 165 µm/s and higher. Just as with Figure 27, on average there is a linear relationship between friction and normal force as expected. There are dramatically larger standard deviations, however, primarily due to topographic artifacts as described above. For example, at a normal force of 1493 nN, the average friction force is 383 ± 267 nN. Therefore, flat samples such as cleaved mica or highly oriented pyrolitic graphite are recommended for the most accurate friction force measurements. At the same time, though, incorporating the full range of data provides new insight into realistic conditions, since practical surfaces are seldom atomically flat. If

more accurate friction measurements are desired on samples with high variations in topography, the approach presented in the next section is more appropriate.

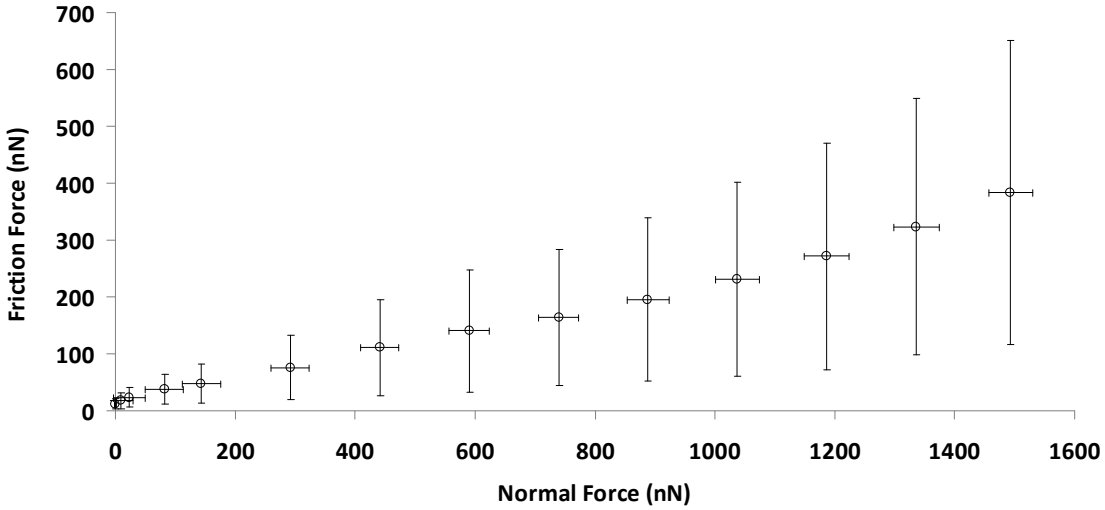

Figure 29: Friction force curve extracted from the top 10% of scan velocities in Figure 28.

3.2 Friction Force Curves with Disabled Feedback Loop

As described previously, instead of attempting to maintain a constant load while scanning a rough surface, the opposite approach can be taken whereby friction data is continuously acquired while the load is allowed to vary by disabling the z-direction feedback loop. Friction force curves were prepared in this manner using a SiN Tetra-17 probe on a TGG01 characterization grating. The normal calibration constant for the cantilever was calculated with force curves and thermal tune to be 67 nN/V. The lateral calibration constant was calculated with the wedge method to be 565 nN/V. The image size used was 9 x 9 µm, and the scanning frequency was 1 Hz. Prior to performing the scan with the disabled feedback loop, a topography image was first collected with the feedback loop

engaged as a baseline and for comparison purposes. Figure 30 presents this topography, including the average cross-section in the image.

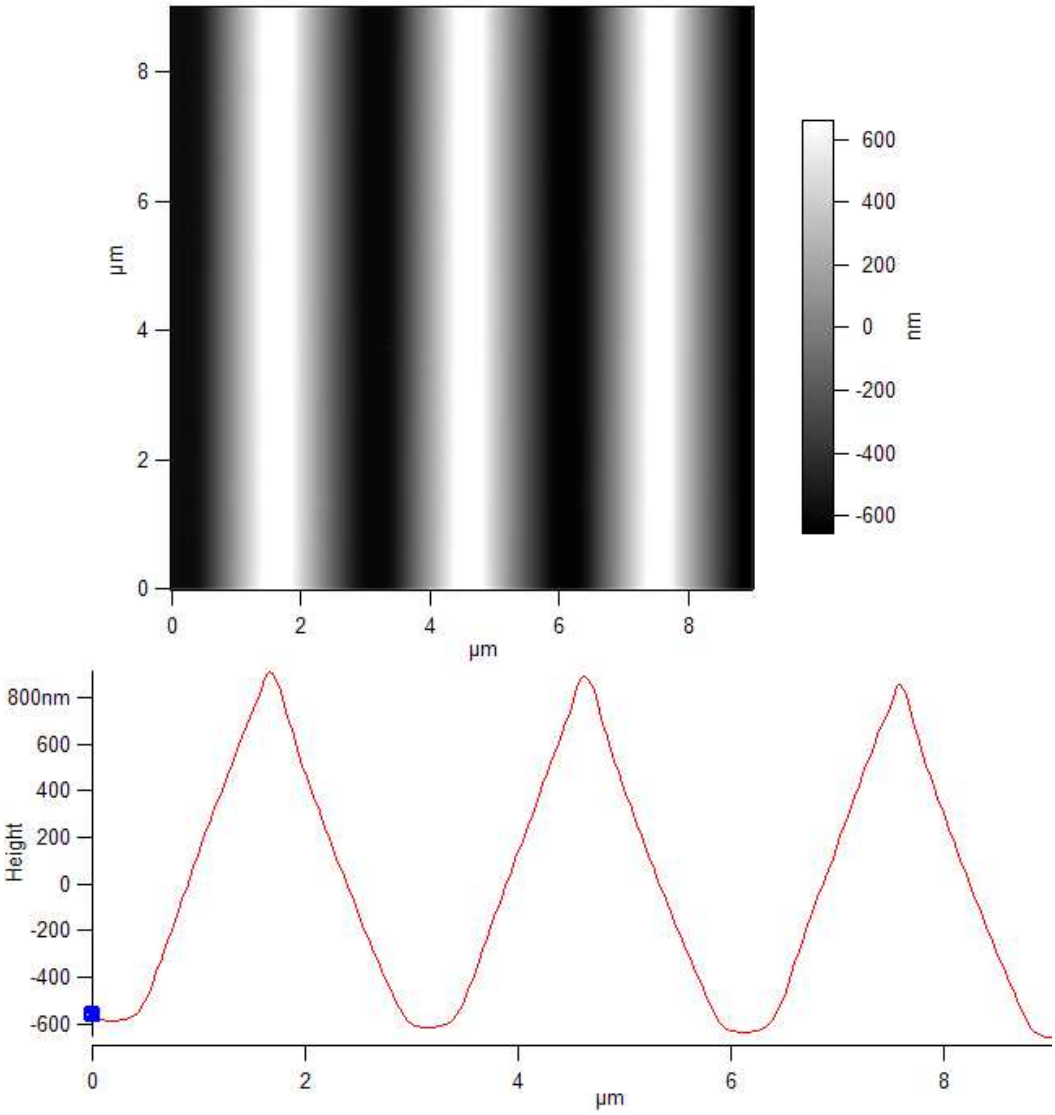

Figure 30: Topography image of TGG01 characterization grating and corresponding cross section. The height of each triangular feature is approximately 1.6 µm. The image was acquired at 1 Hz over a 9 µm scan range using a SiN probe.

The vertical feedback was next disengaged, and an image was acquired recording the deflection and lateral signals. The fast scan axis of the sample movement was perpendicular to the long axis of the cantilever for optimal friction data. Figure 31 presents the lateral signals acquired in this manner.

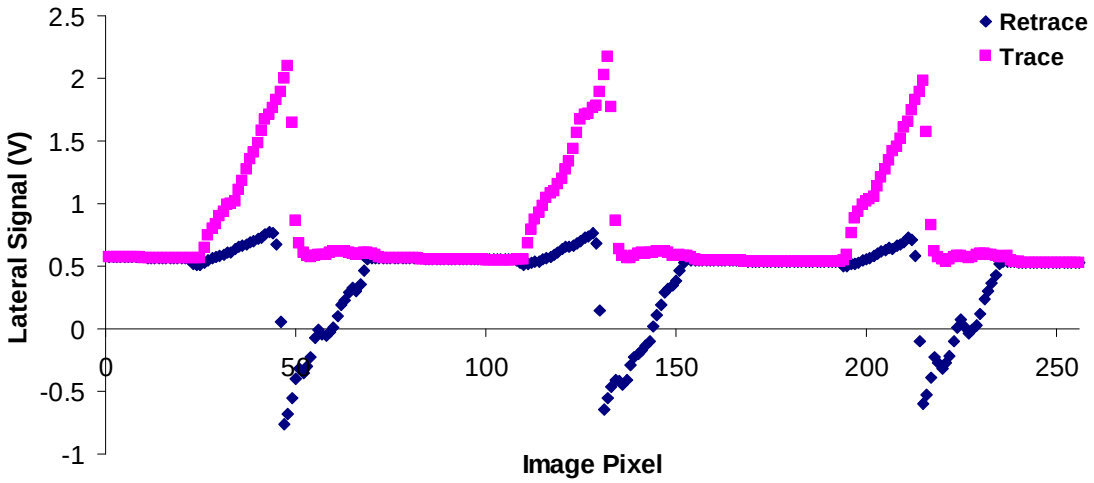

Figure 31: Average lateral signal for each pixel across the fast scan axis. The scan was performed at 10 Hz, 9 µm scan size. The sample was TGG01 characterization grating with SiN probe.

As usual, the trace and retrace signal are subtracted to acquire the friction loop width. This is divided by a factor of 2 to acquire friction in volts. The friction in volts is next converted to force in Newtons, and graphed versus the pixel position in the image (Figure 32). The simultaneously acquired deflection normal force is also overlaid on the plot for comparison. As anticipated, there is no lateral signal when the tip loses contact with deep features on the surface, for instance from pixels 1-25. Otherwise, the friction scales approximately linear with force, again as expected.

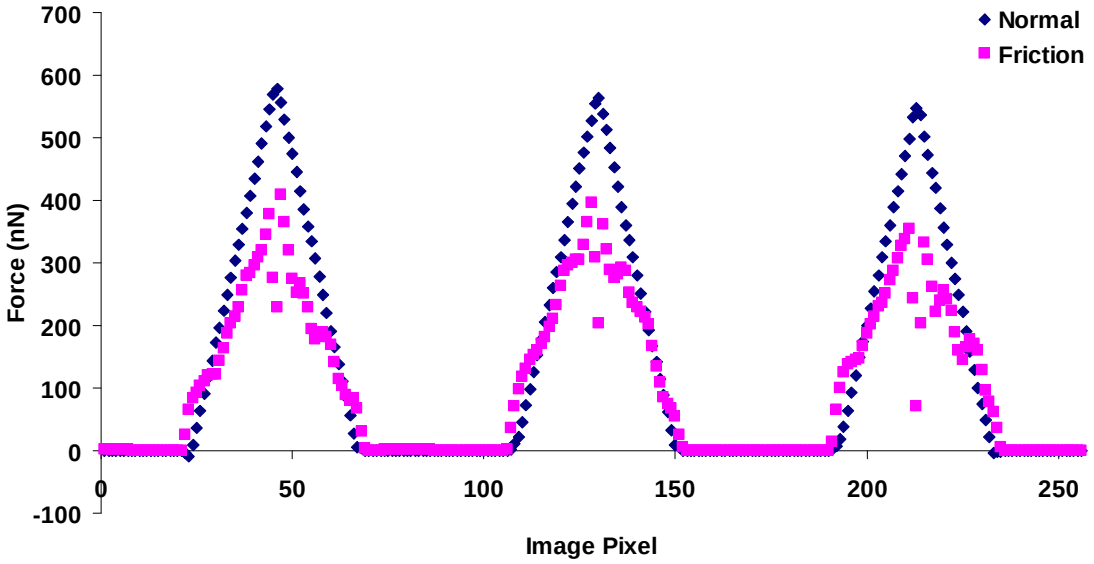

Figure 32: Average normal deflection and friction signal for each pixel across the fast scan axis. The scan was performed at 10 Hz, 9 µm scan size.

Plotting each friction value against its corresponding normal deflection ultimately leads to a no-feedback friction force curve, Figure 33. The slope gives the coefficient of friction as described previously, and the friction at zero force, as well as the pull-off force, can similarly be extracted. The friction at zero force for this cantilever/substrate combination is approximately 70 nN.

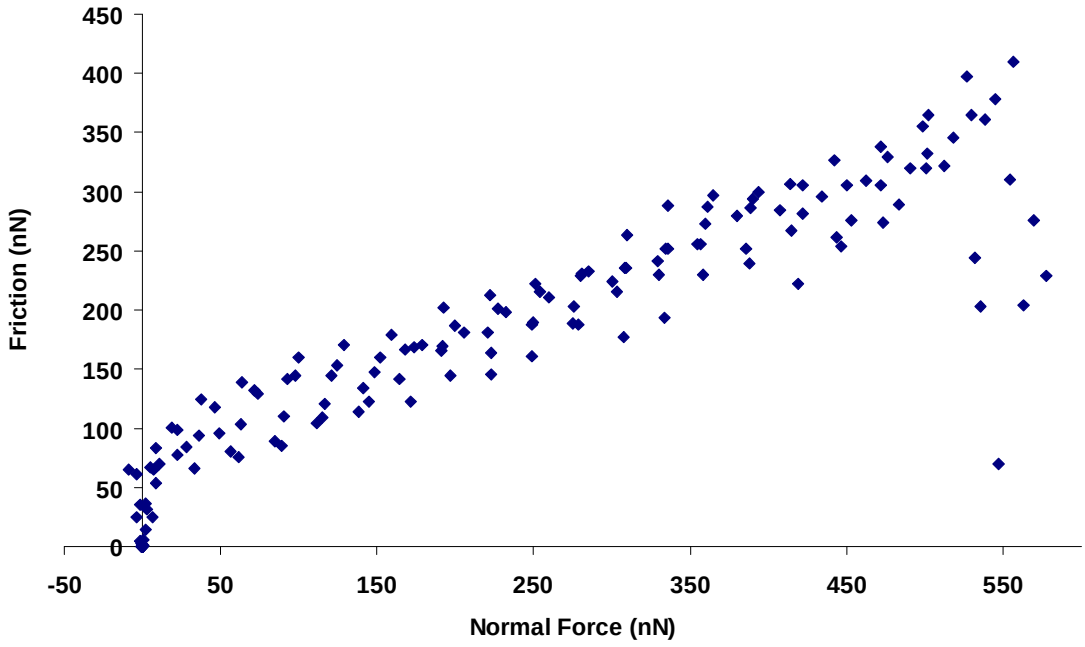

Figure 33: Friction force curve for the SiN probe on TGG01 characterization grating, comprised of the average normal deflection and corresponding friction signal.

One interesting aspect of this data is that at very high normal loads, the friction force appears to decrease substantially. This corresponds to when the AFM tip is climbing over the top of the triangle ridge, and descending down the opposing facet. Since the top of the ridge has a very sharp radius of curvature, the decreased friction force is likely due to a decrease in contact area between the tip and substrate. This very simple approach, based on a single varying force image instead of a sequence of AFM scans with distinct normal loads, again enhances experimental efficiency. It is most appropriate for homogeneous yet rough specimens. For heterogeneous specimens, the newly developed friction force curve mapping method described in the final section is an even better solution.

3.3 High Speed Two-Dimensional Friction Force Curves

All of the measurements in this section were performed with a CDT-FMR-8 diamond coated probe on the SiO_2/thiol/Au substrate, previously discussed in **Chapter 2.5**. The normal calibration constant for the cantilever was calculated with force curves and thermal tune to 292 nN/V. The lateral calibration constant was calculated with the wedge method to 4280 nN/V. Prior to performing any friction measurements, a topography image was acquired. Figure 34 presents the topography of the SiO_2/thiol/Au substrate.

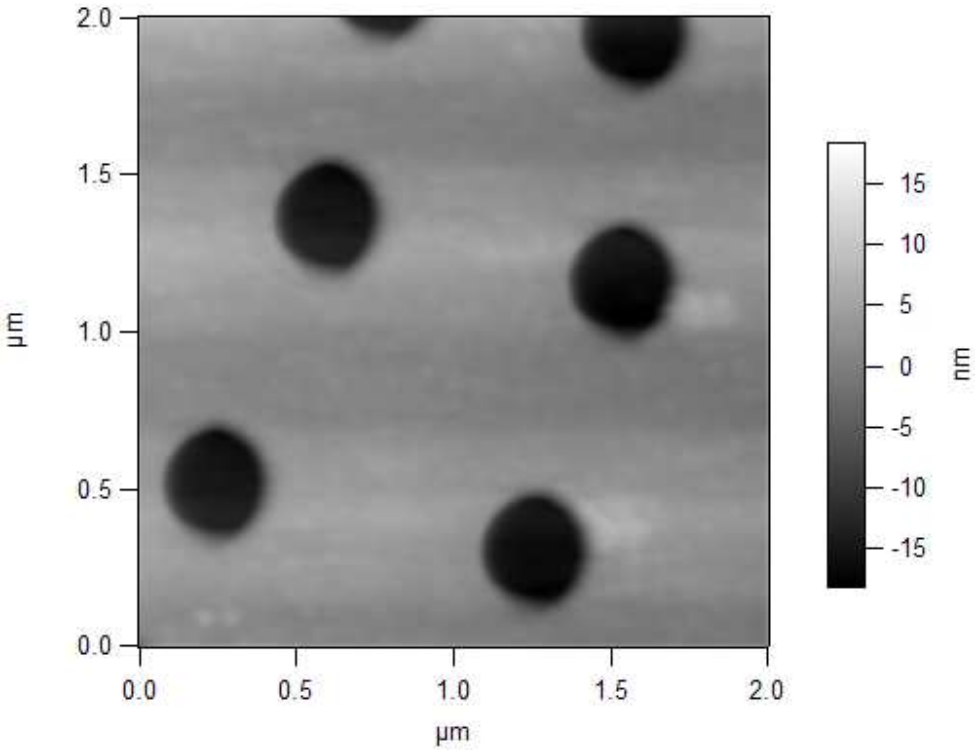

Figure 34: Topography image of the SiO_2/thiol/Au substrate. Diamond probe, 1 Hz, 2 µm scan size.

The goal of the friction force curve mapping approach is to produce maps of topography, coefficient of friction, and friction at zero force for surfaces exhibiting heterogeneous friction properties. To first test whether the SiO_2/thiol/Au substrate is adequate, friction force curves were generated for the SiO_2 and thiol phases by repeatedly scanning a single

line spanning both regions, Figure 35. The initial AFM scan size was 500 x 500 nm, and the lower left quadrant of the circular thiol phase was positioned in the upper right hand corner of an image using AFM scan offset controls. The slow scan axis was then disabled so that friction force measurements would only be acquired along the narrow region highlighted in red. This would ensure that approximately 250 nm of friction data for SiO_2, and 250 nm for thiol, would be collected. A series of friction force measurements were then taken at a 10 Hz line rate, with a deflection set-points decrementing from 654 nN down to -93 nN. A step size of 5.84 nN was used, for a total of 128 friction-force points.

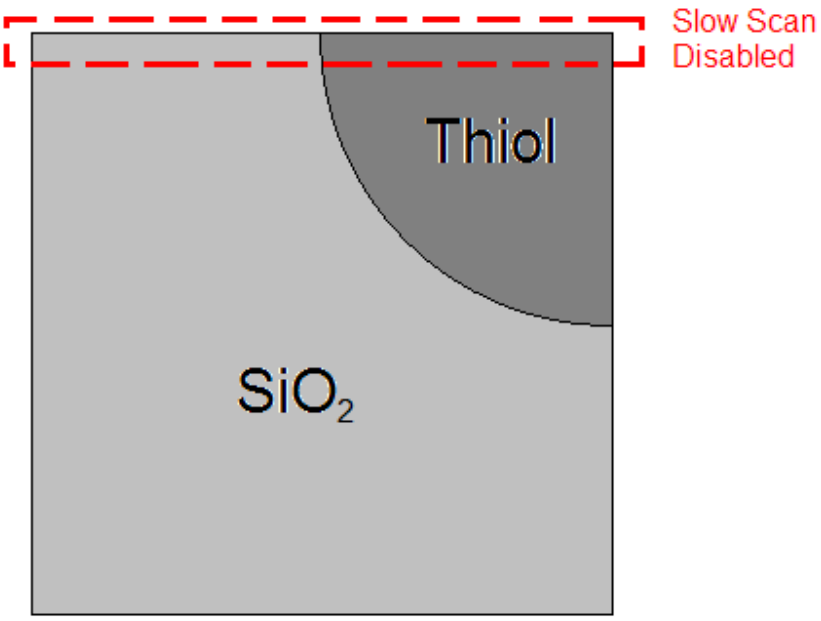

Figure 35: Schematic of SiO_2 and thiol experimental setup for 1-D friction force curve measurement. The slow scan axis of the AFM was disabled to repeat each force measurement on the same line. The scan size was 500 nm, and scan frequency of 10 Hz, with diamond coated probe.

Averaging results from the left half of this data set, and the right half, thus provides distinct friction force curves for the thiol and SiO_2 phases, Figure 36. The friction coefficient (slope), and friction at zero load (offset), are indicated on the figure, clearly

distinguishable for the two specimen regions. The thiol phase has a higher coefficient of friction than the SiO_2 phase, .128 as compared to .084 (a ratio of 1.52:1), and a higher friction at zero applied force, 18.96 nN as compared to 13.37 nN (a ratio of 1.42:1). Therefore, the substrate is a good candidate for developing friction force curve mapping, and extending it to high speed studies.

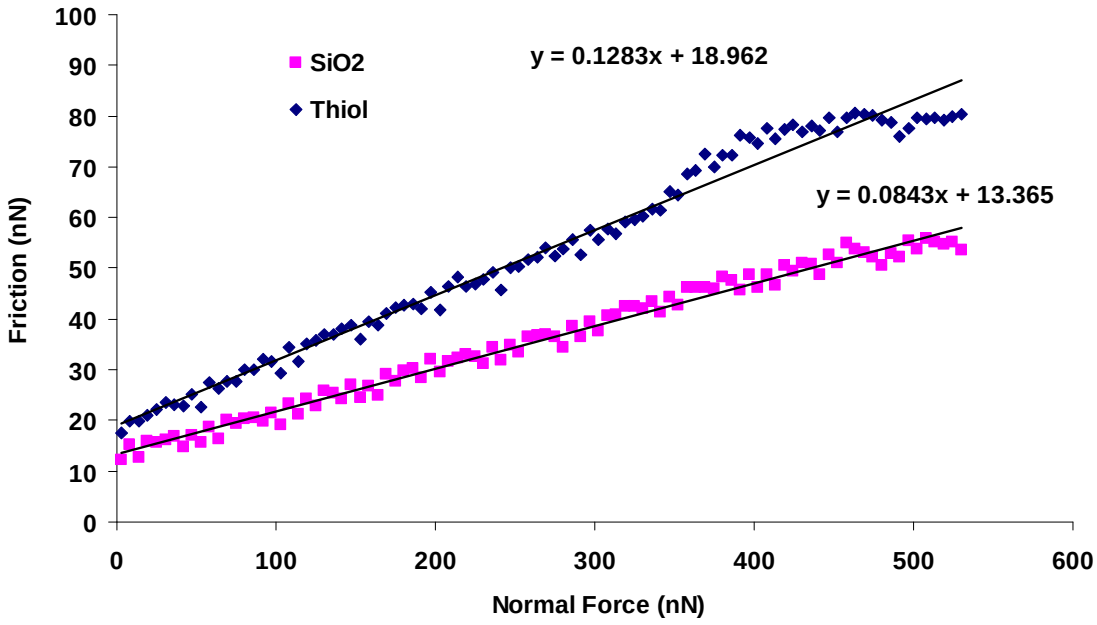

Figure 36: Friction force curves for SiO_2 and thiol. The coefficient of friction for SiO_2 and thiol is 0.128 and 0.084, respectively. Friction at zero applied force for SiO_2 and thiol is 18.96 nN and 13.37 nN, respectively. Data acquired at 10 Hz scanning rates, for comparison with high speed results.

The substrate was also scanned with AC mode and contact mode imaging at a 1 Hz scan frequency and 2 x 2 µm scan size. The phase contrast with AC mode and friction contrast with contact mode were compared to determine which has a higher contrast and resolution, Figure 37 and Figure 38.

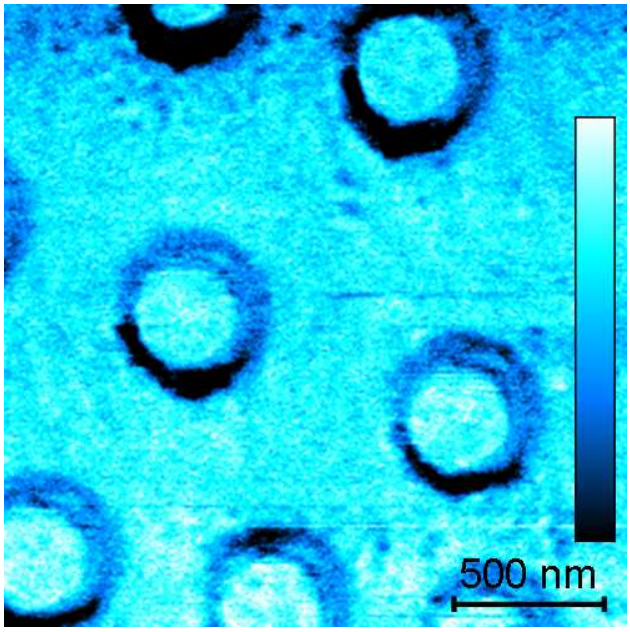

Figure 37: AC mode, phase image of SiO_2/thiol/Au substrate. The scan size and scan frequency is 2 x 2 µm and 1 Hz, respectively. The dark circles represent the phase boundary between thiol and SiO_2.

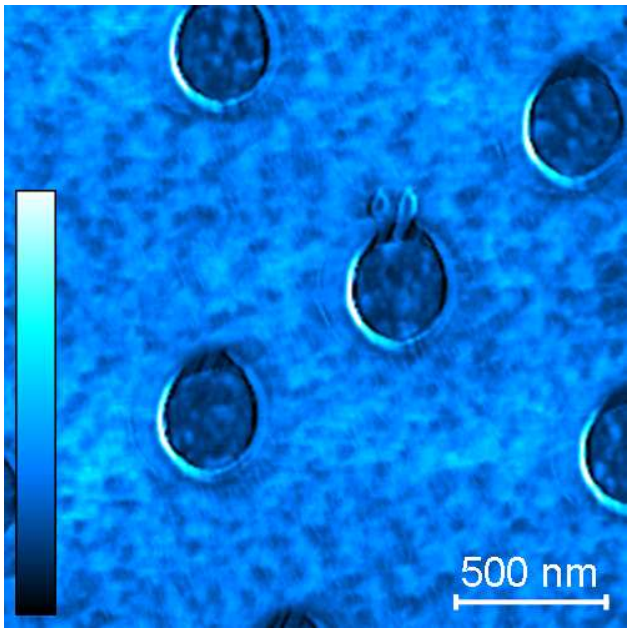

Figure 38: Contact mode, friction image of SiO_2/thiol/Au substrate. The scan size and scan frequency is 2 x 2 µm and 1 Hz, respectively. The dark blue circles represent the thiol phase, and the light blue background represents the SiO_2 phase.

The friction force image (Figure 38) has a distinct higher resolution of phase boundaries between the SiO_2 and thiol as compared to the AC mode phase image (Figure 37). Also, the friction force image has an appreciable difference in contrast between the SiO_2 phase and the thiol phase, whereas the SiO_2 and thiol phase contrast in the AC mode phase image is negligible. The sensitivity of friction force imaging in contact mode appears to be higher than the phase imaging with AC mode. This provides further insight into the alternative use of friction force microscopy for the characterization of phase differences in materials.

For the high speed friction force mapping method, as described previously National Instruments hardware and LabVIEW software was necessary to externally control the piezoactuators and collect data sufficiently rapidly for the fastest scan rates considered. A 1 x 1 µm scan size was selected, along with a scan frequency of 1000 Hz. A sinusoidal wave was applied to the fast scan axis of the piezoactuator, and a triangle wave was applied to the slow scan axis of the piezoactuator. The deflection normal force was then decremented from one high speed image to the next in 29.2 V steps between 765 nN and -23 nN.

In the fast scan (y) and slow scan (x) directions there was a total of approximately 32 nm and 44 nm of drift (8 and 11 image pixels) in the piezoactuator position, respectively (based on topography data). This was corrected prior to extracting the friction force curves by appropriately shifting the image pixels. The trace and retrace signals were then subtracted from one another, converted to force in nN from the as-collected photodetector Volt signals, and used to build up a 3-d stack of friction images where the normal load decreases for each subsequent frame. Drilling along this third dimension thereby provides

62,500 friction force curves, one for each image pixel (technically slightly fewer since a few edge pixels were necessarily cropped to cope with drift during the experiment). A linear fit was applied to each friction force curve to map the coefficient of friction, and the offsets from these fits for each pixel yielded the friction at zero applied force.

In this manner, Figure 39 presents a map of the quantitatively measured coefficient of friction. Subtle variations within the surrounding SiO_2 region are apparent, which would have been averaged out using all previous friction coefficient measuring schemes (appearing instead simply as larger error bars). Sharper contrast occurs at the edges of the thiol-containing pits; this is an artifact related to the abrupt changes in contact area as previously discussed.

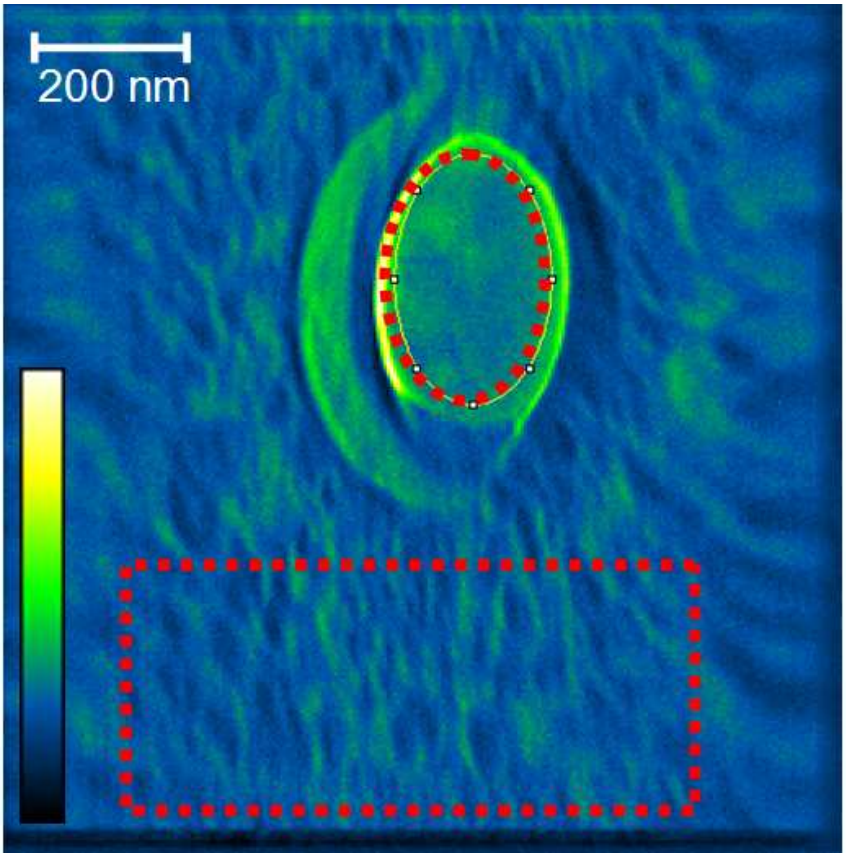

Figure 39: Coefficient of friction for SiO_2 (rectangular region) and thiol (circular region) mapped with high speed two-dimensional friction force curve. The scan size and scan frequency is 1 µm and 1000 Hz, respectively.

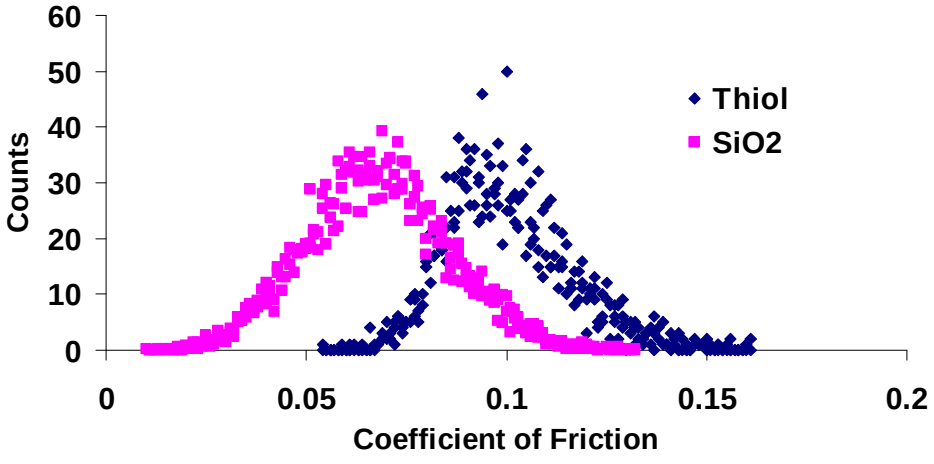

Figure 40: Corresponding histogram of coefficient of friction for SiO2 and thiol regions. The coefficient of friction for SiO_2 and thiol is .068 ± .018 and .101 ± .015, respectively.

Considering the friction coefficient for the SiO_2 compared to the thiol-filled pits, small differences are also apparent. First, the friction within the thiol regions is substantially more uniform. Second, on average it is higher (brighter contrast). Specifically, the coefficient of friction at high scan velocity for the SiO_2 phase is .068 ± .018, while for the thiol phase it is 0.101 ± 0.015 (a ratio of 1.49:1). This is much more clear when histograms of data from these two distinct regions as sketched in Figure 39 are compared, Figure 40. Again, previous approaches would not provide the same depth of data, potentially missing important distinctions in the spatial and frictional distribution. Similarly, Figure 41 presents the map of the friction at zero applied force. More variability within the thiol region is present than for the coefficient of friction, but otherwise the contrast is correlated as anticipated. The top and right edge of Figure 39 and Figure 41 appear black due to the drift correction applied. Both images also have a higher coefficient of friction and friction at zero force to the left of the thiol pit, in the shape of a half-circle. This is likely due to the change in contact area and topography from the silica sphere deposition, coating, and removal process. The diameter of this feature is approximately 500 nm, consistent with the silica sphere diameter.

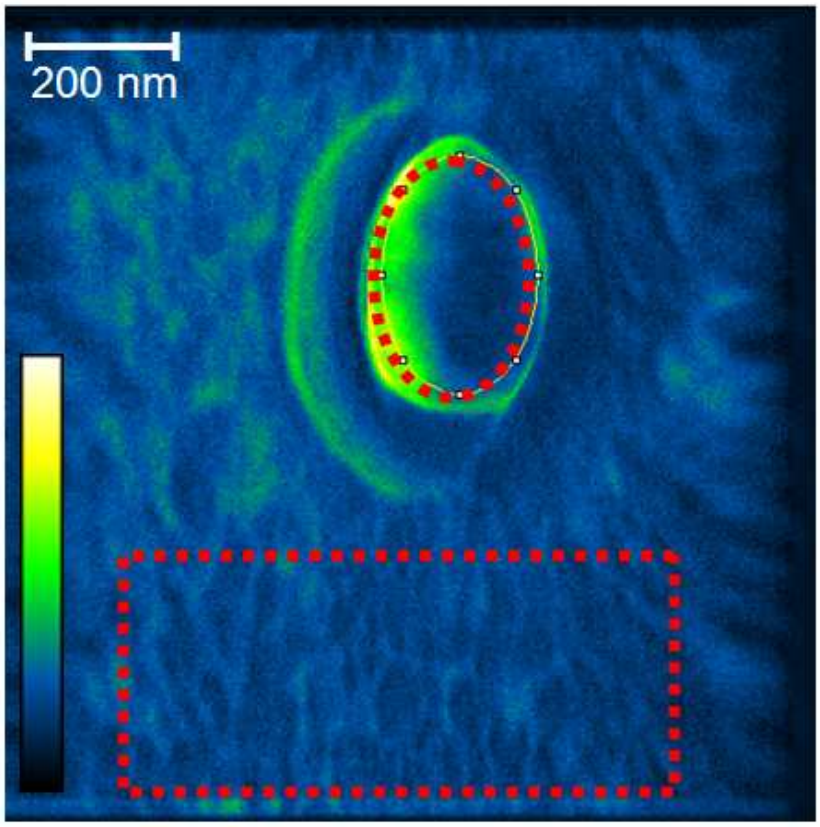

Figure 41: Friction at zero applied force for SiO_2 (rectangular region) and thiol (circular region) mapped with high speed two-dimensional friction force curve. The scan size and scan frequency is 1 µm and 1000 Hz, respectively.

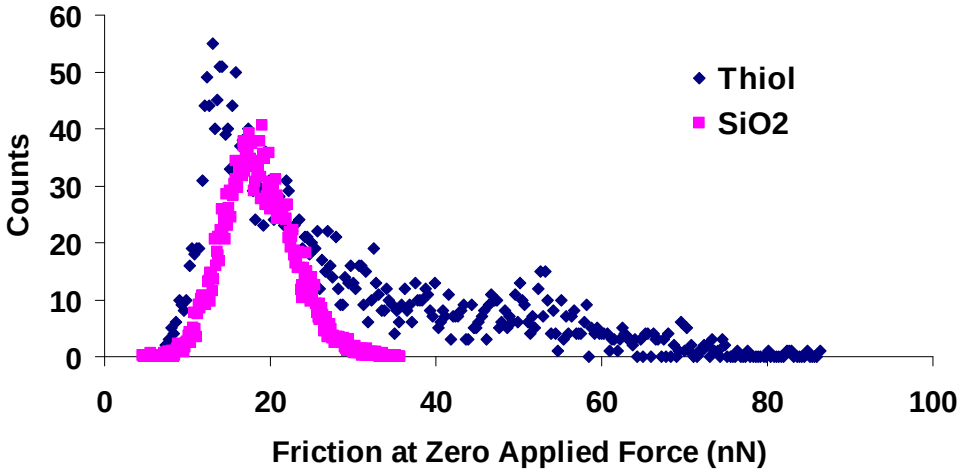

Figure 42: Corresponding histogram of friction at zero applied force for SiO2 and thiol regions. The friction at zero applied force for SiO_2 and thiol is 19.35 ± 4.26 nN and 27.46 ± 15.40 nN, respectively.

Figure 42 depicts zero-force friction histograms from this same data, again separated according to the underlying material for the regions sketched in Figure 41. The friction at zero applied force for the SiO_2 phase is 19.35 ± 4.36 nN. The friction at zero applied force for the thiol phase is 27.46 ± 15.40 nN (a ratio of 1.42:1).

Significantly, the values for coefficient of friction, and the friction at zero applied force, all exhibit the same trend as the more traditional, substantially slower speed, 1-d approach presented in Figure 36. The ratio between coefficient of friction for thiol versus SiO_2 is 1.52:1 for normal (low) scanning velocities, and is 1.49:1 at scanning rates up to 1000 times faster. The ratio between friction at zero applied force for thiol versus SiO_2 for low scanning velocity and high scanning velocity is 1.42:1 and 1.42:1, respectively. This high speed extension to traditional friction mapping is therefore equally accurate. Moreover, the speed enables full friction force curve mapping, an important development for the nanotribology toolbox as it provides nanoscale maps of quantitative friction coefficients. The concept may be applied at standard velocities as well, with appropriate patience, but the results are equally valid at the high rates demonstrated. Besides this enhancement in efficiency, this also provides friction data at more technically relevant sliding speeds, and for surfaces with topographic or phase heterogeneities, as commonly exist in real applications.

Chapter 4: Conclusion

The atomic force microscope is an invaluable tool for the characterization of tribological properties on the micro and nanoscale using lateral force microscopy. Currently, there are no commercially available MEMS or NEMS devices that employ sliding components due to the high adhesion and wear present on such short length scales. Sliding components are used in micro-gears for special applications in energy security and military applications, though. Furthermore, low friction and low adhesion coatings are crucial to the spinning disk data storage industry, and are implemented regularly in more-common latching MEMS structures as well.

One caveat is that nanoscale friction force measurements are traditionally acquired at relatively low scan velocities (< 250 µm/s). The characterization of micro- and nanoelectromechanical devices with increased scan velocities would therefore provide a more realistic view of the friction and adhesion properties relevant to actual device designs. There are currently two systems in use that reach as high as 10 mm/s to 200 mm/s[6, 29], but they are incapable of scanning along two-dimensions and therefore are for diagnostic purposes of homogeneous materials only. For these systems, only the fast scan axis of the sample movement is enabled. This is a serious limitation for resolving friction properties as a function of changing topography, defects, or phases.

In this work, an AFM system is coupled with external hardware and 3 novel imaging approaches are developed and implemented. These enable friction measurements at sliding velocities approaching 20 mm/s, in two dimensions, uniquely providing true, high speed, quantitative friction mapping.

The first new method applies a sinusoidal wave to the fast scan axis of the AFM, enabling efficient friction measurements as a function of velocity, and much higher maximum velocities as compared to traditional scanning methods. The second method rapidly acquires common friction versus force curves, by uncommonly disabling the feedback loop during scanning and relating the resulting lateral data with the correspondingly varying normal loads. The third technique creates a complete 2-d map of friction versus force curves based on a sequence of high speed images each acquired with incrementally lower applied loads. As a result, ‘images’ of the coefficient of friction, friction at zero load, and/or load for zero friction can be uniquely determined with nanoscale resolution for surfaces with heterogeneities in topography, phases, or defects.

4.1 High Speed Sinusoidal Scanning

The practical limit for traditional AFM scanning speeds is related to data acquisition, analysis, and storage rates, challenges which are overcome here through the use of advanced external hardware and software. The absolute limit, on the other hand, is caused by scan-motion-induced excitation of system resonances, contributing to signal noise and ultimately unstable imaging.

By applying a sinusoidal wave instead of the traditional triangle wave to the fast scan axis of the AFM scanners, higher scan velocities are possible than the constant speed approach of normal AFM imaging. The smooth transition between trace and retrace images, instead of discontinuous or even step-like edges with triangle waves, delays the onset of system resonances and hence damaging chattering or vibrations. Furthermore, friction data with a range of velocities can be acquired in a single scan line. Specifically, the center of each line scan for a sinusoidal wave is approximately 60% higher in local

scan velocity than the corresponding triangle wave applied with the same scan size and line rate. The scan edges are correspondingly much lower in tip velocities. By collecting multiple images over the same area with distinct normal loads, friction versus force curves can therefore be quickly extracted for a wide range of scan velocities, saving time and resources.

As an example, the high speed sinusoidal scanning technique was applied to acquire friction properties of a cleaved mica substrate at an upper scanning rate of 18.0 mm/s, the fastest ever recorded in two dimensions. The friction versus the log of scan velocity increases linearly at low velocities (< 2 mm/s) and increases with a higher slope at faster speeds due to viscous damping forces, in agreement with previously published data over atomic instead of um length scales.

The high speed sinusoidal scanning technique was also compared with traditional friction versus force curve measurements on nanocrystalline diamond and cleaved mica substrates. Friction versus force curves were extracted for each substrate at a scan velocity of approximately 165 µm/s. The mica substrate produced higher quality friction properties due to low topographic variation. Samples with high topographic variation require the normalization of normal force, requiring extra calculation time. Therefore, this technique is best suited to measure friction on flat, homogenous samples.

4.2 Friction Force Curves with Disabled Feedback Loop

Friction force curves are acquired to quantify important friction and adhesion parameters such as the coefficient of friction, friction at zero applied force, and pull-off force. Such friction force curves are typically acquired by scanning with a high applied normal force, which is decremented stepwise for each line or image until the AFM tip loses contact

with the substrate. This technique traditionally requires many lines or images of data to be acquired, and does not allow for high speed scanning, especially when the substrate has high variations in topography.

The process of capturing friction force curves in less imaging time, and for higher velocities, can be improved by disabling the vertical feedback loop in the AFM system. As the topography of the substrate changes, the deflection normal force and lateral (friction) forces will increase or decrease. At very low topographic features, the AFM probe will lose contact with the surface, providing adhesion and contact mechanics information. This technique was demonstrated on a TGG01 characterization grating with a soft SiN cantilever. The data collected from a single line scan was sufficient to calculate the coefficient of friction, friction at zero force, and pull-off force for the cantilever/substrate combination. With traditional friction versus force curve measurements, this would take many lines or images to acquire the same force resolution. Ideally, the concept is most relevant for substrates with large changes in topography. If the substrate does not have a high variance in topography, an AFM cantilever with higher stiffness can be selected to provide a higher range of applied normal forces. For atomically flat substrates, i.e. cleaved mica or highly oriented pyrolitic graphite, this technique can still be implemented provided that the substrate is mounted at an angle to produce a sufficient topographic contrast. This technique works best with homogenous samples, but heterogeneous samples can be characterized provided that the areas of interest are spatially recognizable by the subsequent acquisition of an AC mode topography or phase image. For heterogeneous samples, the two-dimensional friction force curves technique is more practical.

4.3 High Speed Friction Force Curve Mapping

Friction force curves are typically acquired on homogeneous substrates where changes in location do not influence the adhesion characteristics. To increase the signal to noise ratio, the data is often acquired by averaging many line scans of data to determine the average friction response of the material. However, characterizing friction with these traditional methods makes it impossible to measure friction as a function of heterogeneities in the substrate, i.e. defects, phases, topography, etc. It is obviously crucial to have a technique capable of quantitatively mapping the influence of heterogeneities on friction, since in many applications the bulk phases do not control the ultimate device performance, but instead the behavior at defects is crucial.

The newly developed high speed friction force curve mapping technique therefore enables the calculation of friction property maps with nanoscale spatial resolution to quantify the influence of topography, phase changes, defects, and other local effects. Multiple images are acquired in a single area, each with a distinct but step-wise decreasing normal force, until the AFM tip loses contact with the substrate. Thereafter, friction versus force curves can be extracted for each pixel, providing the coefficient of friction (slope), friction at zero applied force (offset), and pull-off force. This technique may be applied at high or low scan velocities, depending on the topographic variation of the substrate. The quantitative friction coefficients acquired with this high speed technique are equally valid to those acquired at normal scanning rates, allowing for increased scanning efficiency without sacrificing accuracy.

The images produced with this technique can also be used as an alternative to collecting phase images with standard AC mode, which is notoriously difficult to quantify and

compare for distinct measurements. For a microfabricated SiO_2/thiol/Au substrate considered here, distinct regions and their interfaces are resolved with higher clarity, and reproducible values, when applying the friction force curve mapping approach developed here as compared to standard LFM or AC mode phase imaging. Therefore, this technique is an important development both for characterizing friction properties of heterogeneous substrates more efficiently, and for assessing friction at more technically relevant sliding velocities.

4.4 Experimental Challenges

There are several hardware challenges for high speed work such as this. With respect to AFM, one relates to the piezoactuators and detection systems. For example, as AFM becomes more advanced, the scan sizes and frequencies will continue to increase, allowing for higher velocity friction studies. Currently, the advanced data acquisition card installed in the nmLabs with 4 MS/s is sufficient, but even that will be overcome once a factor of 8 or so in speed enhancements are commonplace. Notably, it is also substantially faster than most commercial AFM systems at present, introducing other difficulties in terms of sufficiently fast data storage, external AFM control and sophisticated software programming (primarily with NI Labview), etc. High speed work requires high bandwidth optical detectors as well, custom components for most commercial AFM systems including the AR Cypher in the nmLabs.

The biggest experimental challenge was consistently defining the upper limit to the piezoactuator scan velocity. As the scan frequency and scan size are increased, the system begins to resonate, translating into vibrations and hence errors in corresponding AFM images. Also, there appears to be an optimal scan size and frequency to achieve a

maximum scan velocity, typically approximately 1000 Hz for the system employed here. As the scan frequency is increased faster than 1000 Hz, the oscillation rate naturally increases, but the distance travelled begins to decrease for the same input amplitude due to LCR effects and roll-off of the electronics specifications. As a result, while the intended scan speed is higher, the absolute scan velocity decreases. For example, theoretically the scan velocity for 2000 Hz is double the velocity for 1000 Hz for an equivalent input scan size. However, we have observed a *decrease* of 43%, 41%, and 47% for 3 µm, 5 µm, and 10 µm scan sizes, respectively, due to loss of efficiency in the actual scanner range. Notably, this effect even varied from day to day, and certainly from sample to sample (since the dynamics depend on the scanner loading, a function of the specimen mass and configuration). This necessitated collection and calibration of the actual scanned distances for all high speed friction data presented herein. The maximum scan velocity achieved in this work, 55 mm/s, was in fact completed with a 1000 Hz scan frequency for a 20 µm scan size on a particularly good day. Unfortunately, the friction properties obtained were erratic due to loss of contact with the surface, so that the highest tip speed for which reliable friction data is reported is in fact approximately 18.0 mm/sec.

4.5 Future Work

For future work, it would be interesting to apply these techniques on a range of substrates other than mica, nanocrystalline diamond, or characterization gratings. For instance, it would be technically relevant to map the friction properties of real MEMS materials or other sliding systems such as spinning disk memory devices (i.e. hard drives).

The friction force curve mapping method, on the other hand, is promising for a far wider range of applications since it can be implemented to study tribology on any substrate with

variations in phase or topography at the nanoscale. Substantially, it does so efficiently, and produces far richer data than single point or line measurements can achieve based on traditional friction force microscopy studies. Given the tremendous important of friction over a wide range of industries and applications, there are consequently many opportunities to implement this new method towards practical and academic goals.

References:

1. The University of the State of New York TSED: **Reference Tables for Physical Setting/Physics.** Albany, NY 12234; 2006.
2. Dowson D: **A Tribological Day.** *Proceedings of the Institution of Mechanical Engineers, Part J: Journal of Engineering Tribology* 2009, **223:**261-273.
3. Grierson DS, Flater EE, Carpick RW: **Accounting for the JKR-DMT transition in adhesion and friction measurements with atomic force microscopy.** *Journal of Adhesion Science and Technology* 2005, **19:**291-311.
4. Maboudian R, Ashurst WR, Carraro C: **Tribological challenges in micromechanical systems.** *Tribology Letters* 2002, **12:**95-100.
5. Maboudian R, Howe RT: **Critical review: Adhesion in surface micromechanical structures.** *Journal of Vacuum Science & Technology B* 1997, **15:**1-20.
6. Zhenhua T, Bhushan B: **New technique for studying nanoscale friction at sliding velocities up to 200 mm/s using atomic force microscope.** *Review of Scientific Instruments* 2006, **77:**103705.
7. Binnig G, Quate CF, Gerber C: **Atomic Force Microscope.** *Physical Review Letters* 1986, **56:**930-933.
8. Meyer G, Amer NM: **Novel optical approach to atomic force microscopy.** *Applied Physics Letters* 1988, **53:**1045-1047.
9. Mate CM, McClelland GM, Erlandsson R, Chiang S: **Atomic-scale friction of a tungsten tip on a graphite surface.** *Physical Review Letters* 1987, **59:**1942-1945.
10. Tabor FPBaD: **The Friction and Lubrication of Solids.** vol. 1. Clarendon, Oxford; 1950.
11. Marti O, Colchero J, Mlynek J: **Combined scanning force and friction microscopy of mica.** *Nanotechnology* 1990, **1:**141-144.
12. Ogletree DF, Carpick RW, Salmeron M: **Calibration of frictional forces in atomic force microscopy.** *Review of Scientific Instruments* 1996, **67:**3298-3306.
13. Sheiko SS, Möller M, Reuvekamp EMCM, Zandbergen HW: **Calibration and evaluation of scanning-force-microscopy probes.** *Physical Review B* 1993, **48:**5675-5678.
14. Munz M: **Force calibration in lateral force microscopy: a review of the experimental methods.** *Journal of Physics D-Applied Physics* 2010, **43**.
15. Cumpson PJ, Hedley J, Clifford CA: **Microelectromechanical device for lateral force calibration in the atomic force microscope: Lateral electrical nanobalance.** *Journal of Vacuum Science & Technology B* 2005, **23:**1992-1997.
16. Li Q, Kim KS, Rydberg A: **Lateral force calibration of an atomic force microscope with a diamagnetic levitation spring system.** *Review of Scientific Instruments* 2006, **77**.
17. J.P. Cleveland SM, D. Bocek, P.K. Hansma: **A nondestructive method for determining the spring constant of cantilevers for scanning force microscopy.** *Review of Scientific Instruments* 1993, **64:**403-405.
18. Sader J E CJWM, Mulvaney P: *Review of Scientific Instruments* 1999.

19. Johnson KL: *Contact mechanics*. Cambridge University Press; 1987.
20. Johnson KL, Kendall K, Roberts AD: **Surface Energy and the Contact of Elastic Solids.** *Proceedings of the Royal Society of London Series A, Mathematical and Physical Sciences* 1971, **324:**301-313.
21. Derjaguin BV, Muller VM, Toporov YP: **Effect of contact deformations on the adhesion of particles.** *Journal of Colloid and Interface Science* 1975, **53:**314-326.
22. Bouhacina T, Aime JP, Gauthier S, Michel D, Heroguez V: **Tribological behavior of a polymer grafted on silanized silica probed with a nanotip.** *Physical Review B* 1997, **56:**7694-7703.
23. Zworner O, Holscher H, Schwarz UD, Wiesendanger R: **The velocity dependence of frictional forces in point-contact friction.** *Applied Physics a-Materials Science & Processing* 1998, **66:**S263-S267.
24. Gnecco E, Bennewitz R, Gyalog T, Loppacher C, Bammerlin M, Meyer E, Güntherodt HJ: **Velocity Dependence of Atomic Friction.** *Physical Review Letters* 2000, **84:**1172-1175.
25. Eyring H: **The Activated Complex in Chemical Reactions.** *The Journal of Chemical Physics* 1935, **3**.
26. Gourdon D, Burnham NA, Kulik A, Dupas E, Oulevey F, Gremaud G, Stamou D, Liley M, Dienes Z, Vogel H, Duschl C: **The dependence of friction anisotropies on the molecular organisation of LB films as observed by AFM.** *Tribology Letters* 1997, **3:**317-324.
27. Santos LV, Trava-Airoldi VJ, Corat EJ, Iha K, Massi M, Prioli R, Landers R: **Friction coefficient measurements By LFM on DLC films as function of sputtering deposition parameters.** *Diamond and Related Materials* 2002, **11:**1135-1138.
28. Tambe NS, Bhushan B: **Friction model for the velocity dependence of nanoscale friction.** *Nanotechnology* 2005, **16:**2309-2324.
29. Tambe NS, Bhushan B: **A new atomic force microscopy based technique for studying nanoscale friction at high sliding velocities.** *Journal of Physics D-Applied Physics* 2005, **38:**764-773.
30. Croft D, Shed G, Devasia S: **Creep, hysteresis, and vibration compensation for piezoactuators: Atomic force microscopy application.** *Journal of Dynamic Systems Measurement and Control-Transactions of the Asme* 2001, **123:**35-43.
31. Leang KK, Devasia S: **Feedback-linearized inverse feedforward for creep, hysteresis, and vibration compensation in AFM piezoactuators.** *Ieee Transactions on Control Systems Technology* 2007, **15:**927-935.
32. Croft D, Devasia S: **Hysteresis and vibration compensation for piezoactuators.** *Journal of Guidance Control and Dynamics* 1998, **21:**710-717.
33. **TGG01 Tip Characterization Grating** [http://www.spmtips.com/tgg]
34. Tseng Q: **Template Matching and Slice Alignment - ImageJ Plugins.** 2012.
35. Prioli R, Rivas AMF, Freire FL, Caride AO: **Influence of velocity in nanoscale friction processes.** *Applied Physics a-Materials Science & Processing* 2003, **76:**565-569.